ADVANCES IN ATMOSPHERIC SCIENCES, VOL. 22, NO. 1, 2005, 69–89

Finite-Time Normal Mode Disturbances and Error Growth During Southern Hemisphere Blocking

Mozheng WEI * and Jorgen S. FREDERIKSEN

CSIRO Atmospheric Research, Aspendale, Victoria 3195, Australia

(Received 18 February 2004; revised 17 August 2004)

ABSTRACT

The structural organization of initially random errors evolving in a barotropic tangent linear model, with time-dependent basic states taken from analyses, is examined for cases of block development, maturation and decay in the Southern Hemisphere atmosphere during April, November, and December 1989. The statistics of 100 evolved errors are studied for six-day periods and compared with the growth and structures of fast growing normal modes and finite-time normal modes (FTNMs). The amplification factors of most initially random errors are slightly less than those of the fastest growing FTNM for the same time interval. During their evolution, the standard deviations of the error fields become concentrated in the regions of rapid dynamical development, particularly associated with developing and decaying blocks. We have calculated probability distributions and the mean and standard deviations of pattern correlations between each of the 100 evolved error fields and the five fastest growing FTNMs for the same time interval. The mean of the largest pattern correlation, taken over the five fastest growing FTNMs, increases with increasing time interval to a value close to 0.6 or larger after six days. FTNM 1 generally, but not always, gives the largest mean pattern correlation with error fields. Corresponding pattern correlations with the fast growing normal modes of the instantaneous basic state flow are significant but lower than with FTNMs. Mean pattern correlations with fast growing FTNMs increase further when the time interval is increased beyond six days.

Key words: normal modes, finite-time normal modes, blocking, tangent linear model, pattern correlations.

1. Introduction

In both the Southern and Northern Hemispheres, numerical weather forecasts during the onset and decay of blocking, frequently suffer from rapid loss of predictability (Bengtsson, 1981; Noar, 1983; Tibaldi and Molteni, 1990; Kimoto, 1992; Anderson, 1993; Tibaldi, 1995; Molteni, 1996). The inability of numerical forecast models to accurately predict blocking transitions is also a limiting factor in producing successful medium and extended range forecasts (Tribbia and Baumhefner, 1993; Colucci and Baumhefner, 1992). Thus, understanding the dynamics and causes of error growth during blocking transitions is of considerable practical importance for both short term and extended range forecasts.

Instability processes of the large scale flow are seen as playing major roles in both the development of blocking anomalies and in the growth of errors during blocking transitions (Frederiksen, 1982, 1984; Simmons, 1983; Frederiksen and Bell, 1990; Borges and Hartmann, 1992; Anderson, 1996; Buizza and Molteni, 1996; De Pondeca, 1998a, b). However, a controversial issue in atmospheric dynamics has been whether disturbances and errors primarily develop as exponentially growing normal modes or whether transient development, involving the interference of superpositions of normal modes, is generally important (Lacarra and Talagrand, 1988; Farrell, 1989; Frederiksen and Bell, 1990; Borges and Hartmann, 1992; Whitaker and Barcilon, 1992; Molteni and Palmer, 1993; Frederiksen, 2000; Frederiksen and Branstator, 2001). This controversy has extended to considerations of the type of perturbations that are most likely to capture the structures of the forecast errors, and that are likely to be useful for constructing initial ensembles for ensemble weather prediction (Palmer, 1993; Toth and Kalnay, 1993, 1997; Houtekamer and Derome, 1995; Molteni,

*E-mail: Mozheng.Wei@noaa.gov

1996; Anderson, 1996; Szunyogh, 1997; Noone and Simmonds, 1998).

Ensemble prediction schemes have recently been implemented at a number of operational weather prediction centers. Singular vectors in the energy norm are used to perturb the control initial conditions at the European Centre for Medium Range Weather Forecasts (ECMWF) (Palmer, 1993; Molteni, 1996). Recently, conditional nonlinear optimal perturbations have been proposed by Mu (2003) and Mu and Duan (2003) to study predictability of atmospheric systems. A "breeding" method is used to construct the initial ensembles at the National Centers for Environmental Prediction (NCEP) (Toth and Kalnay, 1993, 1997) and at the Commonwealth Scientific & Industrial Research Organization (CSIRO) (Frederiksen, 2004). The "bred" perturbations have been likened to Lyapunov vectors, presumably because the leading left Lyapunov vector will emerge from arbitrary initial conditions in integrations of the tangent linear model after a sufficiently long time (Legras and Vantard, 1996; Szunyogh, 1997; Frederiksen, 2000; Wei, 2000). Wei and Toth (2003) and Buizza (2004) provide reviews and comparisons of different ensemble forecast methods currently implemented at world major weather forecasting centers.

Both the singular vector methodology and the "bred" perturbation scheme provide improvements in numerical weather forecasts. This is despite the fact that these two methods use very different perturbations to perturb the control initial conditions. One might wonder whether using still other perturbations would provide further gains in the accuracy of numerical weather forecasts. Recently, it has been suggested that the dominant finite-time normal modes (FTNMs), the eigenmodes of the tangent linear propagator, would characterize the structures and important directions for error growth over a finite time period (Frederiksen, 1997, 2000). FTNMs are norm independent structures (Frederiksen, 2000), unlike singular vectors which depend on the chosen norm, and may be defined for any finite time interval, unlike Lyapunov vectors. FTNMs are the natural generalization of normal modes to time-dependent flows.

Earlier it was proposed that the dominant normal modes of instantaneous flows would approximately characterize the directions of instability and error growth over the next one or two days (Frederiksen and Bell, 1990). Anderson (1996) recently implemented an ensemble prediction scheme for a low order dynamical system in which the control initial conditions are perturbed by superpositions of the dominant normal modes. He found that the normal mode method for his system performed quite well.

Our purpose in this paper is to examine the structural organization of initially random errors evolving in the barotropic tangent linear model. Our particular interest is to compare the structures of evolved error fields with those of the dominant FTNMs and normal modes. We make these comparisons for cases of the Southern Hemisphere blocking in April, November and December 1989.

The plan of the paper is as follows. In section 2, the barotropic tangent linear equations for error growth are summarized. We define FTNMs as eigenmodes of the propagator and compare them with normal modes. A brief discussion of the synoptic situations during the blocking events of April, November, and December 1989 is presented in section 3. There we also describe the construction of the time-dependent basic states obtained from daily analysed 300-hPa streamfunction fields through linear interpolation. In section 4, we study the evolution of initially random errors in April and relate them to the growth and structures of FTNMs and normal modes. The statistics of 100 evolved errors are examined over six-day periods. We calculate probability distributions and the mean and standard deviations of pattern correlations between the evolved error fields and dominant FTNMs and normal modes. Similar studies are performed in sections 5 and 6 for the December and November cases respectively. For November we also consider longer time periods. Our conclusions are summarized in section 7 and the Appendix summarizes details of the iterative eigensolvers used in this study.

2. Theoretical background

2.1 *Models of atmospheric dynamics*

The dynamics of atmospheric flows is frequently studied using models of differing complexity ranging from barotropic models, through quasi-geostrophic models, to multi-level primitive equation models. Formally these models may be written in the form

$$\frac{d\boldsymbol{X}(t)}{dt} = \boldsymbol{N}[\boldsymbol{X}(t)] \,, \tag{1}$$

where $\boldsymbol{N}$ denotes a nonlinear operator. Here, $\boldsymbol{X}(t)$ is the state vector specifying the time-dependent flow in the phase space of either grid point values or spectral components of the dynamical variables. In fact, in this study, the basic state flow will not be taken from a model integration but directly from ECMWF analyses.

Our aim in this work is to examine the evolution of small perturbations growing on analysed basic states. For sufficiently small initial perturbations and for sufficiently short times, the error dynamics is described

by the tangent linear equations (Lorenz, 1965; Lacarra and Talagrand, 1988). These are the equations of motion linearized about the time-varying flow. The observed magnitude of typical forecast errors is such that error growth in weather predictions is linear for several days, depending on horizontal resolution (Errico et al., 1993; Veyre, 1991). At the current rhomboidal $R = 15$ resolution, the tangent linear model is valid for 3 to 4 days for the typical observed errors (Veyre, 1991).

In this paper, we use the tangent linear equations based on the barotropic vorticity equations to describe error growth. Our choice is based partly on simplicity, and on the need to perform large ensembles of simulations. However, it is also the case that a large component of large scale error growth can be described using barotropic dynamics (Veyre, 1991, Frederiksen, 1998).

For flow on a sphere, the nondimensional form of the tangent linear vorticity equation is given by

$$\frac{\partial \zeta}{\partial t} = -J(\psi, \bar{\zeta} + 2\mu) - J(\bar{\psi}, \zeta) - \eta\zeta - \eta' \nabla^4 \zeta \ , \quad (2)$$

where

$$J(\psi, \zeta) = \frac{\partial \psi}{\partial \lambda}\frac{\partial \zeta}{\partial \mu} - \frac{\partial \psi}{\partial \mu}\frac{\partial \zeta}{\partial \lambda},$$

ψ is the streamfunction perturbation, $\zeta = \nabla^2 \psi$ is the vorticity perturbation, while $\bar{\zeta}$ and $\bar{\psi}$ are the basic state vorticity and streamfunction respectively. The other parameters in Eq. (2) are as follows: t is time, λ is longitude, μ is the sine of latitude, and η and η' are the coefficients of viscosity representing drag and diffusion. All the variables are nondimensional with space coordinates scaled by the earth's radius and time scaled by Ω^{-1}, the inverse of the earth's angular velocity.

The results reported here will depend to some extent on the choice of the viscosity used. Therefore, we examine initially both the inviscid case and a case with a typical magnitude of the viscosity, so that comparison of the respective results gives an indication of their sensitivity to dissipation. In the viscous case, typical values of the coefficients of viscosity are chosen as

$$\eta = 8.4 \times 10^{-7} \mathrm{s}^{-1} \ \text{ and } \ \eta' = 2.5 \times 10^{16} \mathrm{m}^4 \, \mathrm{s}^{-1}.$$

The spectral version of the barotropic tangent linear equation is obtained by expanding the streamfunction and vorticity in spherical harmonics. For example,

$$\zeta(\lambda, \ \mu, \ t) = \sum_{m=-R}^{R} \sum_{l=|m|}^{|m|+R} \zeta_{ml}(t) P_{m,l}(\mu) \exp(im\lambda) \ , \quad (3)$$

where R is a rhomboidal truncation wavenumber, which we take to be 15 as in Frederiksen (1997). Here $P_{m,l}(\mu)$ are orthonormalised Legendre functions, m is the zonal wavenumber and l is the total wavenumber. The prognostic spectral equations may then be expressed in terms of $\mathrm{Re}(\zeta_{ml})$ and $\mathrm{Im}(\zeta_{ml})$. With

$$\boldsymbol{x} = [\ldots, \mathrm{Re}(\zeta_{ml}), \ldots, \mathrm{Im}(\zeta_{ml}), \ldots]^{\mathrm{T}}$$

denoting the column vector of real and imaginary parts of ζ_{ml}, the spectral equations can be written in the form

$$\frac{d\boldsymbol{x}(t)}{dt} = \boldsymbol{M}(t)\boldsymbol{x}(t) \ , \quad (4)$$

where

$$\boldsymbol{M}(t) = \frac{d\boldsymbol{N}}{d\boldsymbol{X}}|_{\boldsymbol{X}(t)}$$

is the tangent linear operator evaluated on the analysis trajectory $\boldsymbol{X}(t)$. The formal solution of Eq. (4) is

$$\boldsymbol{x}(t) = \boldsymbol{G}(t, t_0)\boldsymbol{x}(t_0) \ . \quad (5)$$

The propagator $\boldsymbol{G}(t, t_0)$ has an integral representation as given, for example, in equation (2.4) of Frederiksen (1997).

We solve the tangent linear equations with a half-hour time step. The basic states are taken from ECMWF daily analysis and linearly interpolated to obtain the time-dependent fields needed every half hour.

2.2 *Finite-time normal modes*

In the case of time-dependent instability matrices, $\boldsymbol{M}(t)$, the eigenvectors of the propagator, $\boldsymbol{G}(t, t_0)$, play important roles in instability study (Frederiksen, 1997). The eigenvalue equation for $\boldsymbol{G}(t, t_0)$ is

$$[\lambda_\nu \mathbf{I} - \boldsymbol{G}(t, t_0)]\phi_\nu = 0, \quad \nu = 1, \ldots, n, \quad (6)$$

where

$$\lambda_\nu = \lambda_\nu(t, t_0) \ \text{ and } \ \phi_\nu = \phi_\nu(t, t_0)$$

are the eigenvalues and eigenvectors. We call these eigenvectors finite-time normal modes (FTNMs) following Frederiksen (1997). In the above equation, $\boldsymbol{I}$ is the unit matrix. Since the propagator $\boldsymbol{G}(t, t_0)$ maps any initial perturbation from time t_0 to time t, it must carry some important information about the evolution of the basic state $\boldsymbol{X}(t)$, and its eigenvectors must play some role in the error growth from t_0 to t. From Eq. (6), we see that

$$\phi_\nu(t) = \boldsymbol{G}(t, t_0)\phi_\nu = \lambda_\nu \phi_\nu \ . \quad (7)$$

Thus, it is evident that $\lambda_\nu(t, t_0)$ represents the amplification of the perturbation during the period $t - t_0$ and the time-evolving basic state will be unstable if the modulus of $\lambda_\nu(t, t_0)$ is greater than 1.0. The evolved eigenvectors $\phi_\nu(t)$ are also the eigenvectors of $\boldsymbol{G}(t, t_0)$.

If we expand the initial vector $\boldsymbol{x}(t_0)$ in terms of the eigenvectors of $\boldsymbol{G}(t, t_0)$

$$\boldsymbol{x}(t_0) = \sum_{\nu=1}^{n} \kappa_\nu \phi_\nu, \tag{8}$$

then the solution to Eq. (5) is (Frederiksen and Bell, 1990; Frederiksen, 1997)

$$\boldsymbol{x}(t) = \sum_{\nu=1}^{n} \kappa_\nu \lambda_\nu(t, t_0) \phi_\nu, \tag{9}$$

where $\phi_\nu = \phi(t_0)$ and κ_ν are given by

$$\kappa_\nu = \langle \alpha_\nu,\ \boldsymbol{x}(t_0) \rangle / \langle \alpha_\nu\ \phi_\nu \rangle\ . \tag{10}$$

Here $\langle\ ,\ \rangle$ is the Euclidean inner product, and α_ν, the adjoint modes, are the eigenmodes of $\boldsymbol{G}^\dagger(t, t_0)$ with eigenvalues ${\lambda_\nu}^\star$, where $\dagger$ denotes Hermitian conjugate and $\star$ complex conjugate.

Equation (9) indicates that the FTNMs with eigenvalues of larger modulus will dominate the perturbation $\boldsymbol{x}(t)$ for larger $t - t_0$. In the cases of finite-time intervals $t - t_0$, we will use a "recycling" process to filter out the sub-dominant FTNMs as discussed in the Appendix.

We define the growth rate $\omega_{\nu,\mathrm{i}}$ and phase frequency $\omega_{\nu,\mathrm{r}}$ associated with a FTNM through the relationship

$$\lambda_\nu = \lambda_{\nu,\mathrm{r}} + i\lambda_{\nu,\mathrm{i}} = \exp[-i(\omega_{\nu,\mathrm{r}} + i\omega_{\nu,\mathrm{i}})(t - t_0)]\ . \tag{11}$$

Thus

$$\omega_{\nu,\mathrm{i}} = \frac{1}{2(t - t_0)} \ln(\lambda_{\nu,\mathrm{r}}^2 + \lambda_{\nu,\mathrm{i}}^2)\ , \tag{12}$$

$$\omega_{\nu,\mathrm{r}} = \frac{-1}{(t - t_0)} \arctan(\frac{\lambda_{\nu,\mathrm{i}}}{\lambda_{\nu,\mathrm{r}}})\ , \tag{13}$$

where arctan is a multivalued function; its appropriate branch needs to be chosen to specify the phase frequency uniquely. This branch is most efficiently determined by analyzing the phase changes in the FTNMs as they are integrated forward in the tangent linear model.

In the special case when $\boldsymbol{M}(t)$ is independent of time, the propagator has the form

$$\boldsymbol{G}(t, t_0) = \exp \boldsymbol{M}(t - t_0)\ . \tag{14}$$

This may be a reasonable approximation if, over a short time interval, $\boldsymbol{X}(t)$ is slowly varying. The propagator then has eigenvalues

$$\lambda_\nu = \exp \mu_\nu (t - t_0)$$

and eigenvectors ϕ_ν, $\nu = 1, \ldots, n$. Here n is the dimension of $\boldsymbol{X}$, μ_ν are the complex eigenvalues of $\boldsymbol{M}$ and ϕ_ν are the eigenvectors of $\boldsymbol{M}$ which are also called normal modes.

For non-zero and non-degenerate eigenvalues, the eigenmodes form a complete bi-orthogonal system together with the adjoint eigenmodes. The perturbation $\boldsymbol{x}(t)$ will be dominated by the leading normal modes (NMs), which are those associated with the largest real parts of μ_ν, when $t \gg t_0$. The non-leading modes will gradually become irrelevant with increasing time (Frederiksen and Bell, 1990). This filtering process is further discussed in the Appendix.

3. Synoptic situations and observed basic states

Blocking highs derive their name from the fact that they are quasi-stationary features that tend to occur in preferred geographical locations and block, or deflect

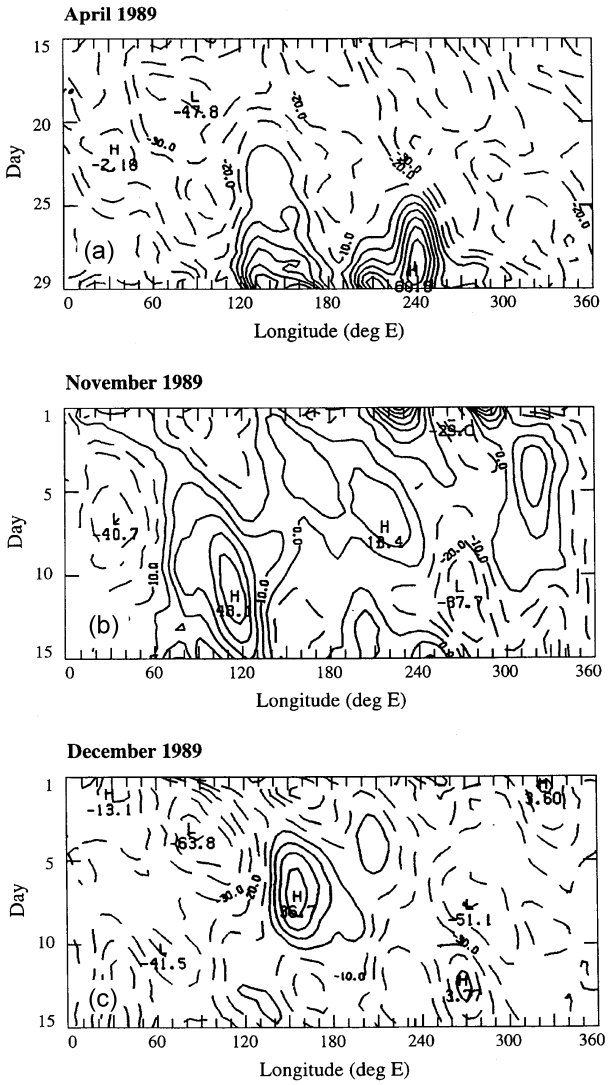

Fig. 1. Hovmoeller diagrams of blocking indices in 1989 in the Southern Hemisphere for (a) the second half of April, (b) the first half of November, (c) the first half of December.

towards the pole, the normal eastward progression of weather systems. During their growth, amplification and decay they tend to be associated with a loss of predictability.

In this study we examine error growth associated with developing blocks that formed in the regions of Australia-New Zealand or in the Central Pacific in April, November and December 1989. As noted in a number of observational studies (e.g., van Loon, 1956; Wright, 1974; Coughlan, 1983; Lejenas, 1984), the Australian-New-Zealand region is the primary preferred region for blocking action in the Southern Hemisphere. The blocking indices for these three months are shown in Fig. 1. The daily Hovmoeller diagrams for the second half of April and the first halves of November and December are shown in Figs. 1a–c respectively. These indices are based on observations and taken from the Climate Monitoring Bulletin of the Australian Bureau of Meteorology (CMB, 1989). Their definition of the blocking index (BI) for the Southern Hemisphere is as follows:

$$I_{\mathrm{B}} = 0.5(U_{25\mathrm{S}} + U_{30\mathrm{S}} + U_{55\mathrm{S}} + U_{60\mathrm{S}} - U_{40\mathrm{S}} - U_{50\mathrm{S}} - 2U_{45\mathrm{S}}) , \quad (15)$$

where U denotes the 500 hPa zonal wind at the latitudes indicated by subscripts.

During late April, blocking high-low dipoles formed at the longitudes of eastern Australia and in the central Pacific. These events are associated with positive blocking indices around 150°E and 240°E between 24 April and the end of the month (Fig. la). The eastern Australian block was preceded by a large amplitude trough that developed to the southwest of Western Australia around 20 April. This blocking dipole caused a splitting of the jet stream into two distinct currents as it amplified. This is seen in Fig. 2a, which shows the streamfunction for the flow at 300 hPa at 0000 UTC on 24 April. The blocking dipole is equivalent barotropic and, as usual, is more evident at lower levels (not shown). By 26 April, the block had moved downstream to a location near New Zealand and started to decay. This was also the time when the central Pacific block began its development near 240°E. These events are seen in Fig. 2b, which shows the 300 hPa streamfunction at 0000 UTC on 26 April.

For April (also for November and December), we shall focus on barotropic processes associated with 300 hPa basic states, which is why we have concentrated on this level in the above discussion even though the blocks are more evident at lower levels. The reasons for choosing the 300 hPa level for analyzing barotropic processes relate to theoretical arguments that show that a higher level than the traditional 500 hPa one is appropriate for barotropic model studies (Held, 1983; Simmons, 1983).

During November 1989, blocking activity was above average from east of 0 degrees longitude to the central Pacific. Our interest is focussed on the blocking dipole that formed early in the month near 120°E, as shown by the blocking index in Fig. 1b. The block started developing around 8 November and a blocking dipole pattern extending through the troposphere became established over the Indian Ocean on about 11 November. As a consequence, the jet stream was split into two quite distinct branches across the Indian Ocean, as seen at 0000 UTC on 12 November in Fig. 2c, which shows the 300 hPa streamfunction. Towards the middle of the month, the block moved downstream and decayed.

In early December, a blocking high pressure system began developing over the southernmost extent of the Tasman Sea between Australia and New Zealand. The corresponding positive blocking index near 150°E is shown in Fig. lc. By 0000 UTC on 9 December, a large amplitude blocking dipole extended through the troposphere as shown in the 300 hPa streamfunction field in Fig. 2d. The block subsequently decayed after 10 December.

Our basic states are constructed from daily 300 hPa streamfunction fields at 0000 UTC during the three periods discussed above. We linearly interpolate to obtain the time-dependent fields needed every half hour in simulations and theoretical studies. Because our basic states are constructed from analyses based on observations, they include all effects acting on the atmosphere including diabatic heating, baroclinic and topographic effects. In theory, it is desirable to examine the full instability properties of atmospheric states based on the complete flow equations. However, the full non-hydrostatic primitive equations are extremely difficult to analyze and even they would rapidly diverge from the observed atmospheric trajectory.

4. Error growth during April

In this section, we examine the growth of initial random errors evolving in the barotropic tangent linear model during April 1989. We examine how quickly the random errors become organized by the tangent linear dynamics and we analyze their evolved structures. We first present a case study of the evolution of a particular initial random error field and then examine the statistics of the growth of 100 random error fields.

4.1 *A case study of error growth*

Here, we examine the evolution of an initial, randomly generated error field during the period from 20 April to 26 April. Throughout this paper, all dates

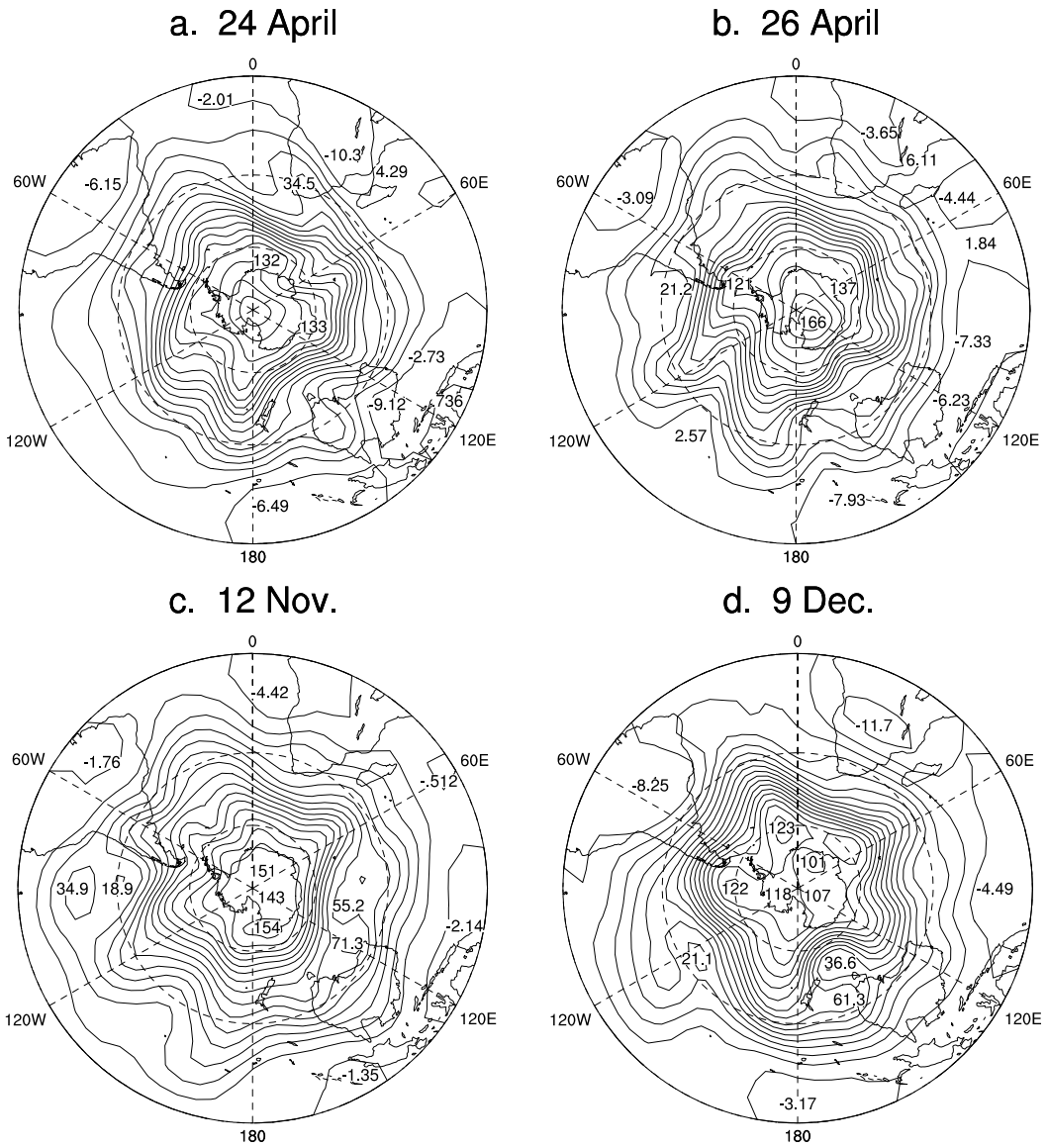

Fig. 2. The basic state streamfunction (in $km^2\ s^{-1}$) at 300 hPa on (a) 24 April, (b) 26 April, (c) 12 November, (d) 9 December in 1989.

specified refer to the time of 0000 UTC unless stated otherwise. The 300 hPa streamfunction for the initial random error field starting on 20 April is shown in Fig. 3a, and the evolved error fields on 24 and 26 April are shown in Figs. 4a and 4b respectively. These results are for the inviscid tangent linear dynamics. The diagrams show that, at these times, the error field has been organized by the tangent linear dynamics to take up large scale structures. These dipole or multi-pole structures have similar scales to the blocking disturbances. They occur in the respective blocking regions and extend downstream.

The large scale dipole error structure started developing near 120°E on 23 April (not shown) and amplified as it moved downstream into the blocking region between Australia and New Zealand on 24 April (Fig. 4a). On 25 April, the large scale error structure moved eastward to the region between 180° and 120°W and rapidly amplified as the block in the central Pacific developed (not shown). The error field further amplified and took up a wave train structure in the blocking region between 60° and 120°W on 26 April (Fig. 4b). In all these cases the evolved error field has a dipole or multi-pole structure of similar scale to the developing block.

We next compare these evolved error fields with

dominant normal modes and FTNMs for the case of inviscid dynamics. Both the normal modes and FTNMs described in this section have been calculated using the iterative Arnoldi method described in the Appendix. First, we consider the dominant normal mode of the instantaneous basic state taken as the 300 hPa streamfunction at 1200 UTC on 25 April 1989. The 300 hPa streamfunction of this mode is shown in Fig. 3b in arbitrary units; it has a wave train structure in, and extending downstream of, the blocking region in the South Pacific near 120°W. It is a stationary mode with an e-folding growth time of 2.41 days. Modes with very similar structure are also found at other times around this period including mode 2 (the second fastest mode) at 0000 UTC on 25 April, mode 3 at 1200 UTC on 24 April and mode 1 at 0000 UTC on 26 April. This last mentioned mode, however, is located slightly further downstream.

Normal mode 1 in Fig. 3b has a qualitatively similar wave train structure in the sector between 60°W and 120°W to that of the evolved error field on 26 April (Fig. 4b). This finding is consistent with the idea that during block development (and other rapid developments) the dominant normal modes of the instantaneous flows would, to a first approximation, characterize the structures of instability and error growth over the next one or two days (Frederiksen and Bell, 1990; Frederiksen, 1998). Frederiksen (1997, 2000) argues that dominant FTNMs may provide a more accurate representation of the structures of evolved errors. We examine next the structures of the dominant FTNMs.

We have calculated FTNMs for the time-dependent basic state for different periods all starting on 20 April and finishing on or before 26 April. Figures 4c and 4d display the structures of the dominant FTNM for the periods of 4 and 6 days starting on 20 April and finishing on 24 and 26 April respectively. Table 1 shows the real (λ_r) and imaginary (λ_i) parts of the eigenvalues of the dominant FTNMs during 20 to 26 April. Also shown are their amplification factors ($|\lambda|$), dimensional growth rates ($\omega_{d,\,i}$) and e-folding times (τ).

From a comparison of the adjacent diagrams in Fig. 4, it is evident that the evolved error field takes up a structure that is very similar to that of the corresponding first FTNM in the respective key blocking regions. This is due to the fact that the tangent linear dynamics filters the disturbances in favor of the dominant FTNMs (Eq. (9)). This filtering tends to increase with increasing time periods as described by Frederiksen (1998). For example, for the period 20 to 26 April, $|\lambda_1| = 8.2$, $|\lambda_2| = 5.6$, $|\lambda_3| = 4.3$, $|\lambda_4| = 3.9$,

Table 1. Nondimensional real (λ_r) and imaginary (λ_i) parts of eigenvalues, amplification factors ($|\lambda|$), the dimensional growth rates ($\omega_{d,\,i}$) and e-folding times (τ) of FTNM 1 during 20-26 April 1989 (inviscid case).

Basic state	λ_r	λ_i	$\lvert\lambda\rvert$	$\omega_{d,\,i}$ (d^{-1})	τ (d)
20–21	1.323	0.0	1.323	0.284	3.52
20–22	–1.439	0.812	1.653	0.250	4.00
20–23	1.857	–0.967	2.093	0.245	4.08
20–24	3.079	–1.459	3.407	0.305	3.27
20–25	4.843	0.0	4.843	0.314	3.18
20–26	–6.842	4.439	8.156	0.349	2.86

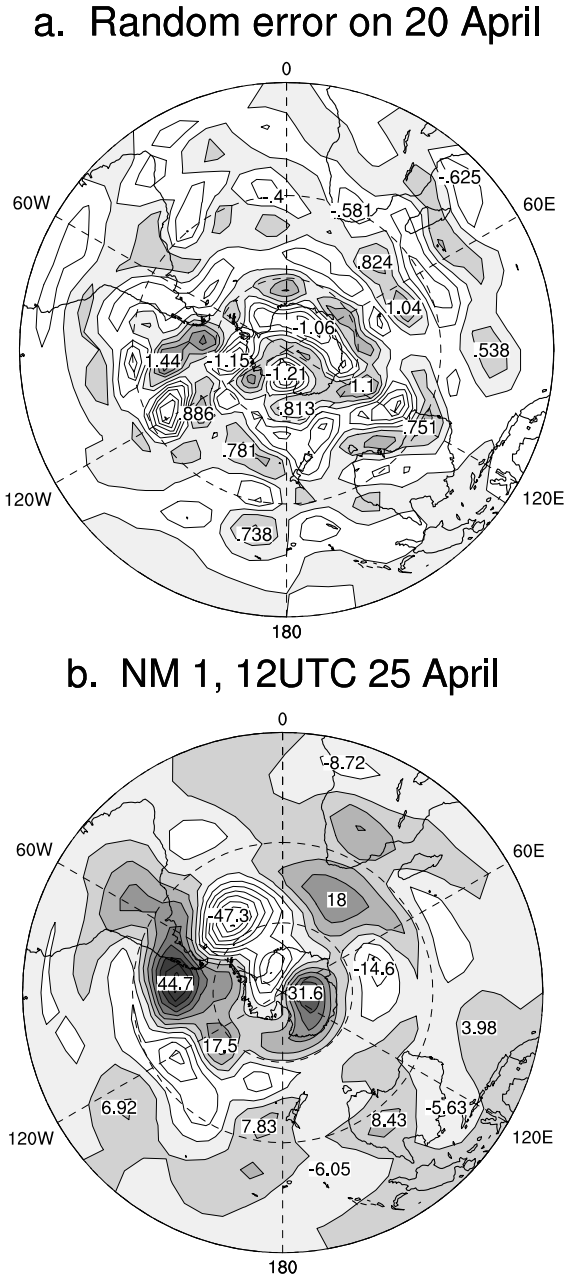

Fig. 3. (a) The 300 hPa streamfunction for a randomly generated initial error field on 20 April 1989. (b) The 300 hPa streamfunction of normal mode 1 at 1200 UTC on 25 April 1989.

$|\lambda_5| = 3.8$ and $|\lambda_6| = 3.3$. As well, some of the dominant FTNMs have somewhat similar structures in the key blocking regions.

Our findings in this subsection for Southern Hemisphere blocking, relating error fields to the structures of dominant normal modes and FTNMs, are consistent with the results of similar case studies for Northern Hemisphere blocking (Frederiksen, 1997, 2000). What is not known, however, is how representative these case studies are. We consider this question next by considering the statistics of the growth of 100 random error fields.

4.2 *Statistics of ensemble error growth*

In this subsection we analyze the statistics of the growth of 100 initial, randomly generated error fields. The initial random perturbations are chosen from a Gaussian distribution in which the magnitudes of the streamfunction spectral coefficients are proportional to $(2l+1)^{-1}$; that is, $|\psi_{ml}| \sim 1/(2l+1)$. This means that $\sum_m |\psi_{ml}|$ is exactly constant in the inner rhomboid where $l \leqslant R$ and falls off with total wavenumber in the oute rhomboid. It also means that the total

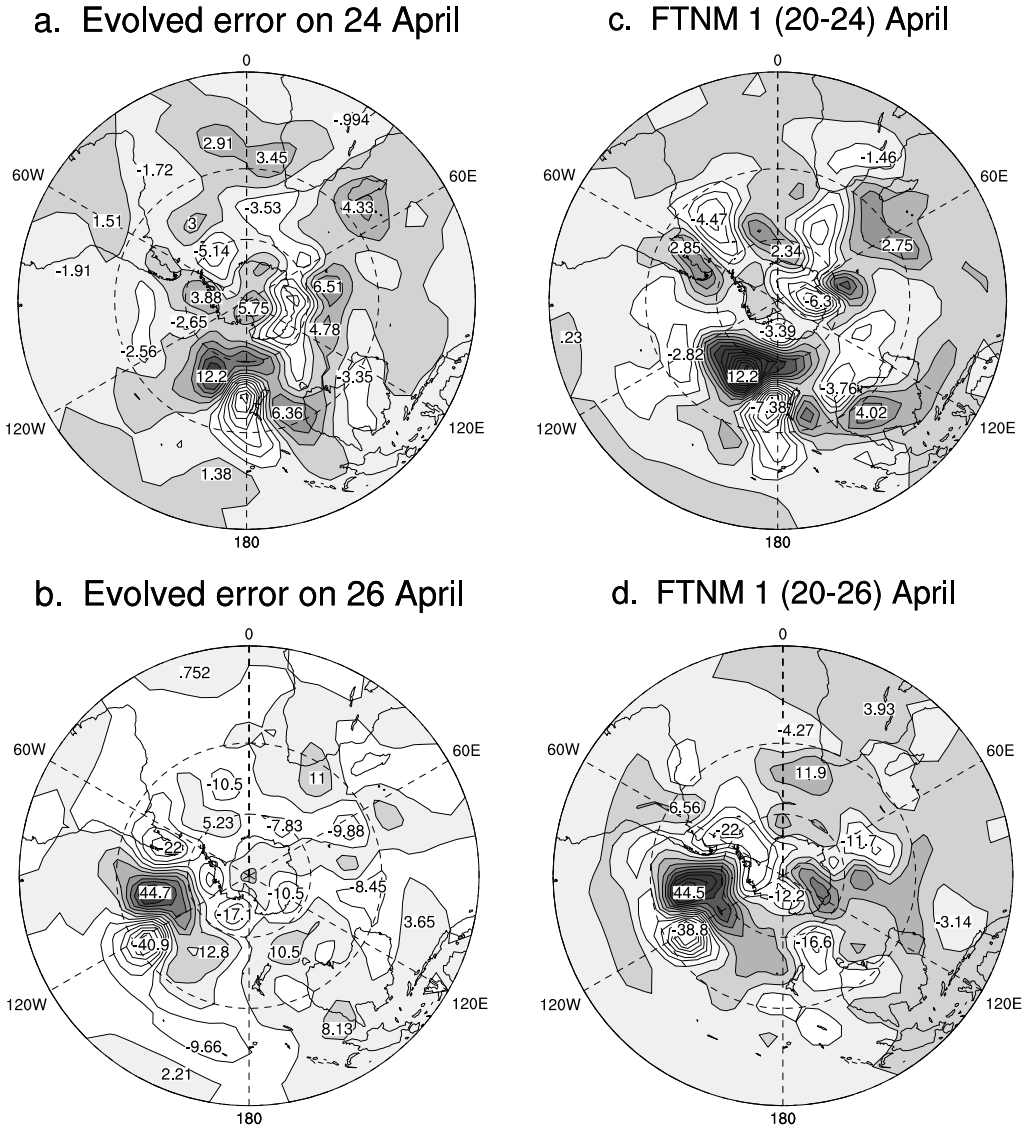

Fig. 4. The streamfunctions of evolved random errors and FTNM 1 during the period between 20 to 26 April 1989 in the inviscid case. The evolved errors are shown on (a) 24 and (b) 26 April. Also shown are FTNM 1 from 20 to (c) 24 and (d) 26 April. The magnitudes and phases of FTNM 1 have been chosen to be closely similar to the evolved errors (c.f. Appendix).

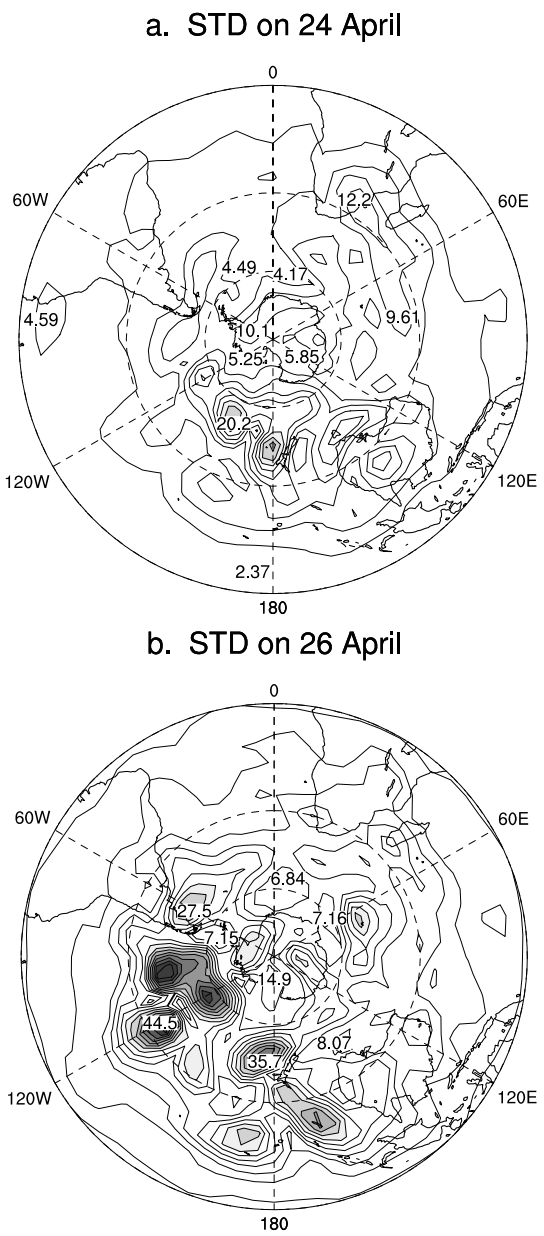

Fig. 5. The standard deviations of 100 evolved error fields on (a) 24 April and (b) 26 April.

wavenumber spectrum of kinetic energy,

$$e(l) = \sum_m l(l+1)\psi_{ml}\psi^*_{ml} \ ,$$

increases linearly in the inner rhomboid and falls off with wavenumber in the outer rhomboid. There are uncertainties in the determination of the analysis error covariance matrix. However, the linear increase of the total wavenumber spectrum of kinetic energy in the inner rhomboid to $l = R = 15$ and fall off in the outer rhomboid appears to be consistent with typical estimates of 2-day forecast errors as seen in Fig. 4d of Molteni (1996); their spectrum for differences between ECMWF and Deutsche Wetterdienst (i.e., German Weather Service) analyses is however flatter. Each perturbation is evolved in the tangent linear barotropic model from 20 to 26 April. We first consider the case of inviscid dynamics, and calculate the standard deviations of the 100 error fields on each day. These are shown on 24 and 26 April in Figs. 5a and 5b respectively. A comparison with the case study in Fig. 4 shows that the case study is a very representative example; on each day the amplitude of the error field in Fig. 4 is located in regions of large standard deviation. The standard deviation in Fig. 5, however, also shows some extra regions of development, particularly near the dateline on 26 April.

Next, we consider the changes in the amplification factors as the errors grow. We define the inner product of any two real Southern Hemisphere physical space streamfunction fields $X(\theta,\rho,t)$ and $Y(\theta,\rho,t)$ at time t by

$$\{Y(\theta,\rho,t), X(\theta,\rho,t)\} = \frac{1}{2\pi}\int_0^{2\pi} d\theta \int_{-1}^{0} d\rho Y(\theta,\rho,t)X(\theta,\rho,t), \qquad (16)$$

where θ is longitude and ρ is sin(latitude). Then the amplification factor for a perturbation field $X(\theta,\rho,t)$ over a time period from t_0 to t is

$$A_{\rm f}(t,t_0) = \frac{\{X(\theta,\rho,t), X(\theta,\rho,t)\}^{\frac{1}{2}}}{\{X(\theta,\rho,t_0), X(\theta,\rho,t_0)\}^{\frac{1}{2}}}. \qquad (17)$$

Figure 6 summarizes our results for the increases in the amplification factors with time as the 100 initial random perturbations grow. In Fig. 6a, we show $A_{\rm f}$ for 20 of the perturbations; these 20 were the first of the 100 that were chosen by our random number generator. Also shown in Fig. 6a is the amplification factor for FTNM 1 for different time periods starting on 20 April and finishing on the day indicated. We note that for all but one of the 20 first perturbations, the amplification factors on a given day are smaller than for FTNM 1. In fact, this exception is the only outlier among the 100 error fields that exceeds the FTNM 1 amplification factor at any stage. Figure 6a also shows the mean of the amplification factors for the first 20 perturbations (indicated by □). The variations in the amplification factors of the error fields are reflections of the projections of the initial errors onto FTNM 1.

For the inviscid case, we depict, in Fig. 6b, the mean (thin solid) of the 100 amplification factors of the error fields and, as well, the mean ± the standard deviation (thin dashed) of the 100 amplification factors. Also shown in Fig. 6b are the corresponding results for the viscous case (respective thick lines).

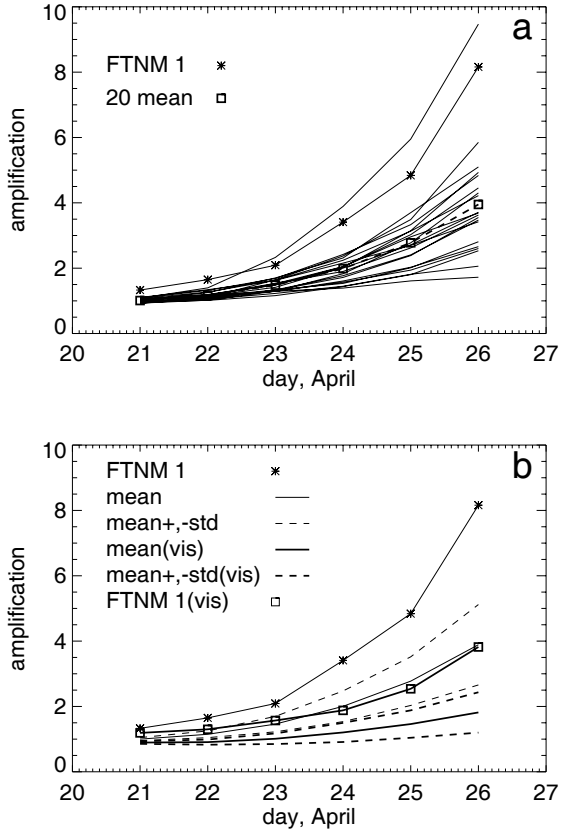

Fig. 6. The amplification factors of FTNM 1 and evolved errors in both inviscid and viscous cases during periods from 20 to 21, 22, ..., 26 April 1989. (a). The first 20 of the 100 evolved random errors (solid lines), FTNM 1 in inviscid case (∗) and the mean of the first 20 evolved random errors (□). (b). Inviscid case: FTNM 1 (∗), the mean of 100 evolved errors (thin solid line) and mean ± standard deviation of 100 evolved errors (thin dashed lines). Viscous case: FTNM 1 (□), the mean of 100 evolved errors (thick solid line) and mean ± standard deviation of 100 evolved errors (thick dashed lines).

Figure 6b again shows the amplification factor for FTNM 1 in the inviscid case and, as well, in the viscous case. We note that both the mean and mean + standard deviation of the amplification factors of the error fields on a given day are smaller than for FTNM 1 in the respective inviscid and viscous cases. As expected, viscosity reduces the amplification factors of both the error fields and FTNMs. For the FTNMs, this may be seen in more detail by comparing the inviscid results for eigenvalues, amplification factors and growth rates in Table 1 with the corresponding viscous results in Table 2.

Our particular interest in this subsection is in determining the statistics of pattern correlations (calculated over the Southern Hemisphere) between the random perturbations and the FTNMs. Here the pattern correlation between any two real physical space streamfunction fields $X(\theta,\rho)$ and $Y(\theta,\rho)$ is defined by

$$A_{\rm c} = \frac{\{Y,X\}}{\{Y,Y\}^{\frac{1}{2}}\{X,X\}^{\frac{1}{2}}}\ , \qquad (18)$$

We note that the structure of FTNMs may change with time or phase (for generalized traveling FTNMs; Frederiksen and Branstator, 2001, Appendix). We therefore calculate the pattern correlation ($A_{\rm c}$) at the phase of the FTNM that gives the largest $A_{\rm c}$. The mean (solid) and mean ± the standard deviation (dashed) of the pattern correlations between each of the 100 error fields and FTNMs are displayed in Fig. 7. Figure 7a shows these quantities for the largest correlations taken over the five fastest growing FTNMs and for both the inviscid (thin lines) and viscous (thick lines) cases. The largest correlation is calculated as follows. For each error field at time t, we calculate the pattern correlation with each of the five fastest growing FTNMs for the period t_0 to t and take the largest of these five pattern correlations. Then, we calculate the mean and mean ± standard deviations over 100 error fields. Figure 7b depicts the corresponding results for the correlations between the error fields and FTNM 1 in the inviscid (thin lines) and viscous (thick lines) cases. For the viscous case, Fig. 7c gives the corresponding results involving FTNM 2 (thick lines) and 3 (thin lines), while the results corresponding to FTNM 4 and FTNM 5 are shown in Fig. 7d in thick and thin lines respectively.

In Fig. 7a, the mean and the mean ± the standard deviations increase monotonically with time and there is little difference between the inviscid and viscous cases. This contrasts with the situation for correlations with individual FTNMs in Figs. 7b–d, which increase in general with time but also show local variability. We note in particular that FTNM 1 generally, but not always, gives the largest average pattern correlations with the error fields. For example, FTNM 1 and FTNM 3 appear to swap roles on 24 April in the viscous case. Qualitatively similar results for the sub-

Table 2. Nondimensional real ($\lambda_{\rm r}$) and imaginary ($\lambda_{\rm i}$) parts of eigenvalues, amplification factors($|\ \lambda\ |$), the dimensional growth rates ($\omega_{\rm d,\,i}$) and e-folding times (τ) of FTNM 1 during 20–26 April 1989 (viscous case).

Basic state	$\lambda_{\rm r}$	$\lambda_{\rm i}$	$\|\ \lambda\ \|$	$\omega_{\rm d,\,i}$ ($\rm d^{-1}$)	τ (d)
20–21	1.190	0.0	1.190	0.174	5.757
20–22	–1.136	0.628	1.230	0.129	7.704
20–23	1.428	–0.650	1.569	0.149	6.691
20–24	1.884	0.0	1.884	0.158	6.337
20–25	0.232	–2.527	2.538	0.186	5.387
20–26	–3.284	1.951	3.820	0.223	4.492

dominant modes are obtained in the inviscid case (not shown). From Figs. 7a and b, we might also expect that the average correlation taken over the five fastest growing FTNMs and the mean correlation with FTNM 1 would increase further if the time interval were increased beyond six days. We consider this question in section 6.

Next, we consider probability distributions of correlations between the 100 evolved error fields on 26 April and FTNMs for the period 20 to 26 April. We compare these with corresponding probability distributions where the correlations involve normal modes of the instantaneous basic state at 0000 UTC on 25 April instead of the FTNMs. Our purpose is to examine whether FTNMs are more likely predictors of the structure of evolved errors than normal modes. That this should be the case has been suggested by the work of Frederiksen (1997, 1998) and the case study in subsection 4.1. Figure 8a shows the probability distribution for the largest correlations taken over the five fastest growing FTNMs, and the probability distribution for the largest correlations taken over the five fastest growing normal modes is shown in Fig. 8c. Figure 8b shows the probability distribution for the correlations with FTNM 1, the same is shown for normal mode 1 in Fig. 8d. Both diagrams are for the viscous case; very similar results are found for the inviscid case (not shown).

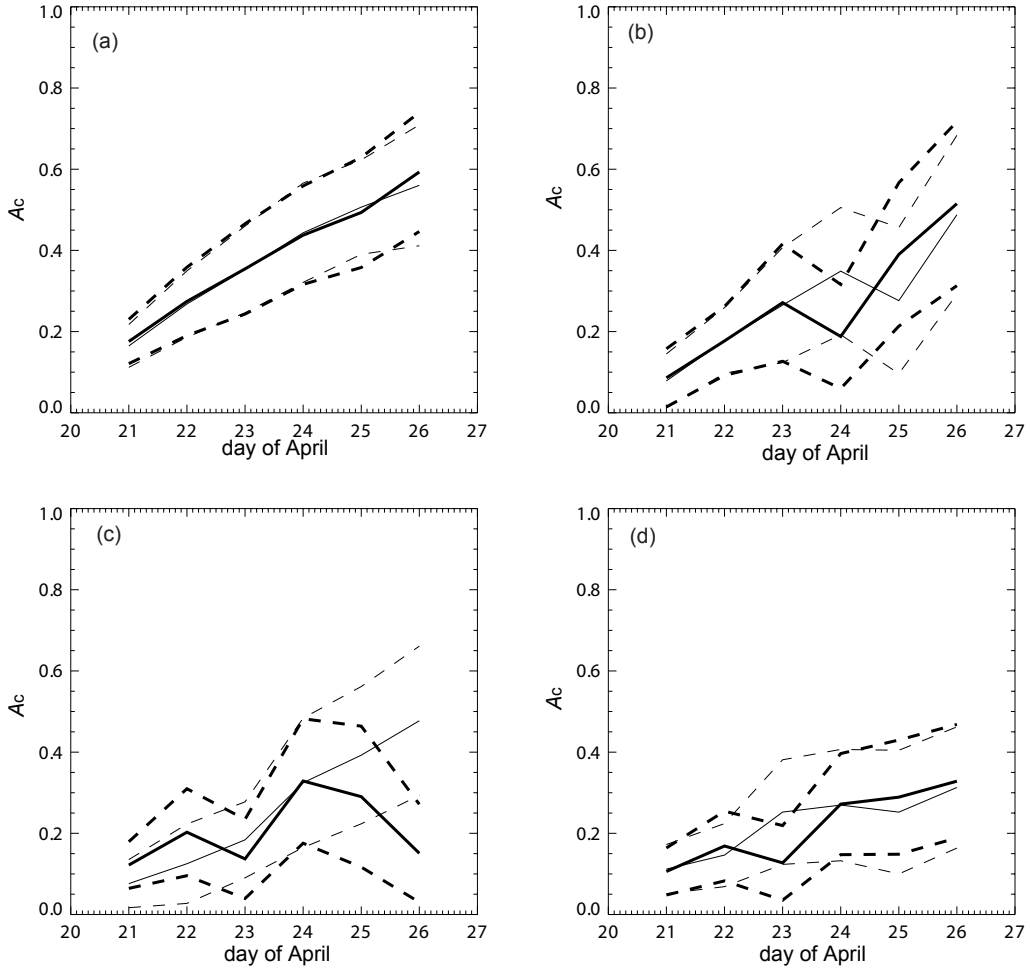

Fig. 7. Pattern correlations (A_c) between the dominant FTNMs and the 100 evolved random errors in both inviscid and viscous cases during the periods from 20 to 21, 22, ..., 26 April 1989. (a) The mean (solid) and mean ± the standard deviation (dashed) of the largest correlations taken over the five fastest growing FTNMs (viscous — thick, inviscid — thin). (b) As in (a) but for the correlations between the 100 evolved random errors and FTNM 1. (c) The mean (solid) and mean ± the standard deviation (dashed) of the correlations between the 100 evolved random errors and FTNM 2 (thick) or FTNM 3 (thin). (d) As in (c) but for FTNMs 4 and 5 respectively.

It is clear that there is considerable spread in the correlations for the 6-day period ending on 26 April. However, the correlations taken over the five fastest growing FTNMs and the correlations with FTNM 1 are generally high. The average correlation taken over the five fastest growing FTNMs is about 0.6, and the mean correlation with FTNM 1 is slightly over 0.5 (Figs. 7a and b). The correlations taken over the five fastest growing normal modes and the correlations with normal mode 1 tend to be lower than with the respective FTNMs. They are nevertheless significant and indicate that it may be possible to obtain a reasonable representation of evolved error fields through expansions in terms of a subset of the faster growing normal modes (Frederiksen and Bell, 1990; Anderson, 1996; Frederiksen, 1998).

The results in this section, both with and without viscosity, have shown that initial random errors tend to evolve to structures similar to the dominant FTNMs, especially FTNM 1, and particularly for longer time periods. The growth rates of initially random errors are generally bounded by the growth rate of the dominant FTNM. Only one out of 100 random initial errors has been found to grow faster than the dominant FTNM during the period from 20 to 26 April. In the next two sections, we examine the generality of our findings for other cases of block development.

5. Statistics of ensemble error growth in December

In this section we consider, rather briefly, the statistics of the evolution of random errors for early December when the blocking high developed over the southernmost extent of the Tasman Sea. The synoptic situation was somewhat similar to that when the east-

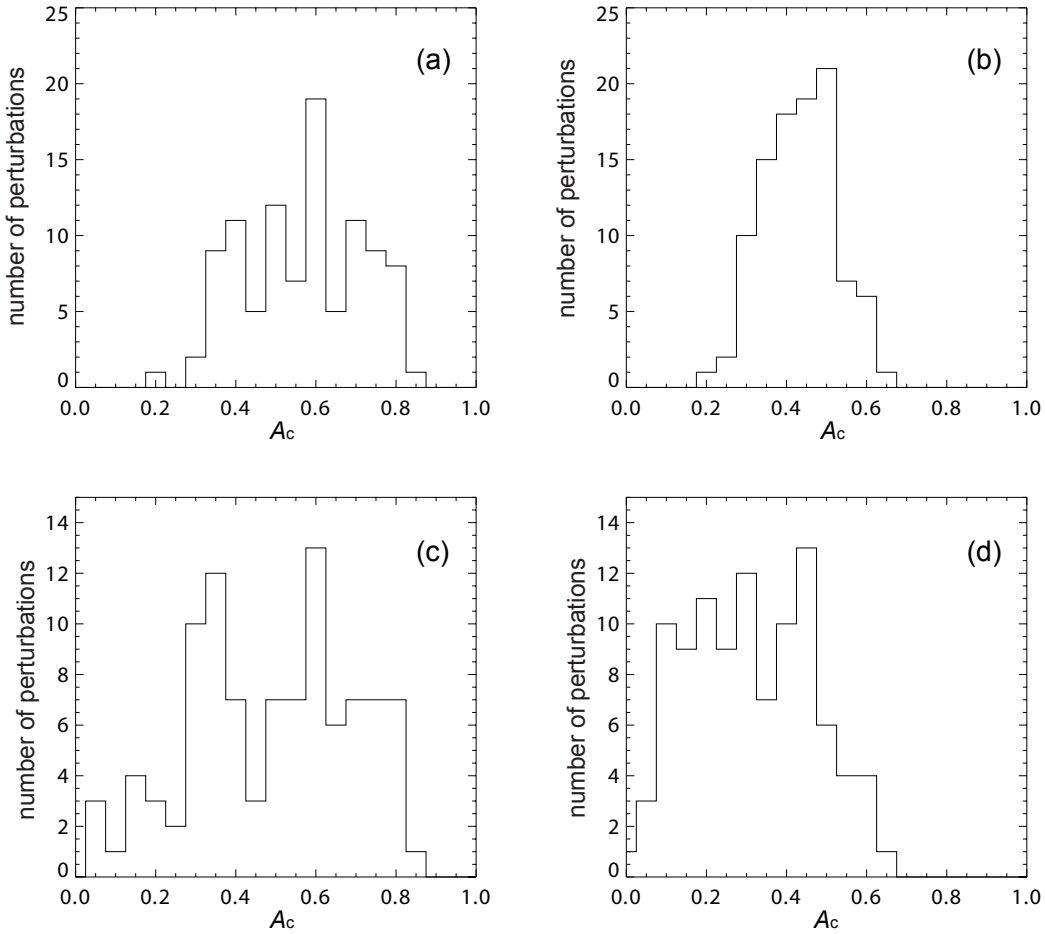

Fig. 8. The probability distributions of correlations between the 100 evolved random errors on 26 April and FTNMs for the period 20 to 26 April for the viscous case. (a) Shown are the probability distributions for the largest correlations taken over the five fastest growing FTNMs. (b) The probability distributions for the correlations with FTNM 1. (c) The same as (a), but taken over the five fastest growing normal modes. (d) The same as (b), but for normal mode 1.

ern Australian block developed in April. Then, in section 6, a more detailed discussion of error growth during November will be given. For the remainder of this paper we focus on the case of viscous dynamics.

For December, we again analyze the statistics of the growth of 100 initial randomly generated error fields, constructed as described in section 4. We study error growth during the period from 5 to 11 December, which covers the development, maturation and decay of the Tasman Sea block. The 100 initial random perturbations are generated on 5 December and the standard deviations of the 100 evolved error fields are calculated on each day and shown on 9 and 11 December in Figs. 9a and 9b respectively. As the block developed in the sector between 120°E and 180°E, the standard deviation of the error fields was also concentrated in this region (Fig. 9a). Then, as the block moved downstream and started to decay, the error field amplified near the dateline (Fig. 9b). We again see a focusing of errors in regions of rapid dynamical development.

Figures 9c and 9d also show the fastest growing FTNMs for the periods 5–9 and 5–11 December respectively. They are large scale wave train structures with significant amplitudes in the regions where the error fields are concentrated. Table 3 lists the eigenvalues, amplification factors, growth rates and e-folding times for the fastest growing FTNMs during the period 5–11 December. We find that the amplification factor for

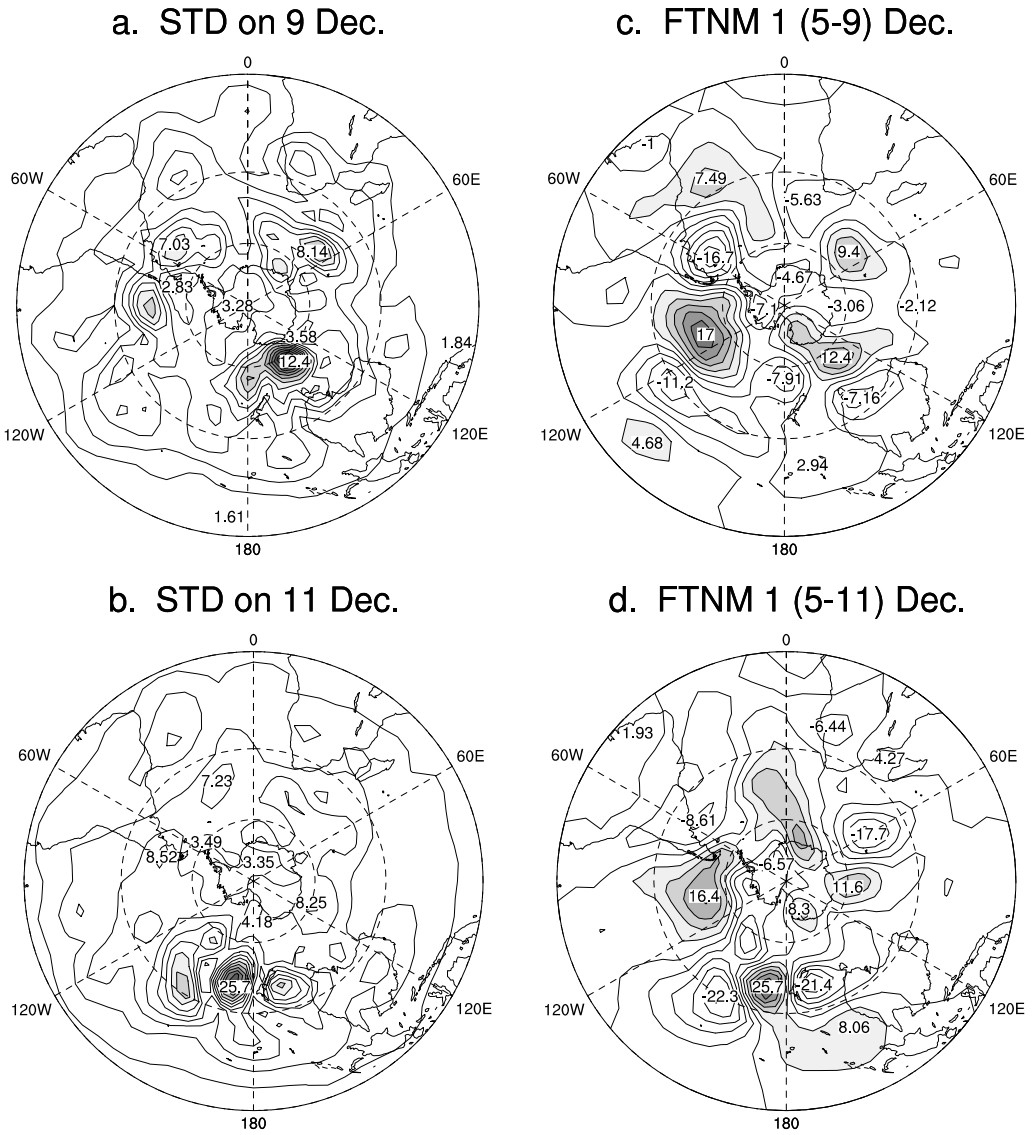

Fig. 9. The standard deviations of the 100 evolved random errors on 9 December (a) and 11 December (b) 1989 for the viscous case. Shown are FTNM 1 for the periods 5–9 December (c) and 5–11 December (d) 1989 in the viscous case.

each of the 100 evolved error fields is comparable with, but slightly smaller than, that of the corresponding dominant FTNM on each day (not shown).

Figure 10 shows the mean (solid) and mean ± the standard deviation (dashed) of the pattern correlation between each of the 100 error fields and FTNMs on successive days between 5 and 11 December. Figure 10a depicts these statistics for the largest correlations taken over the five fastest growing FTNMs. Figure 10b displays the corresponding statistics for correlations between error fields and FTNM 1 (thick lines) and FTNM 2 (thin lines) respectively. In Fig. 10a, as in Fig. 7a, the statistics increase monotonically with time. In contrast, from Fig. 10b it appears that FTNM 1 and FTNM 2 swap roles on 8 and 9 December in that FTNM 2 yields larger pattern correlation statistics than FTNM 1.

6. Error growth during November

Next, we examine the statistics of the development of random errors during the second week of November when a blocking dipole pattern became established over the Indian Ocean. The period of interest is between 8 and 14 November. We also study the growth of initial random errors for the longer period stretching from 1 to 15 November. Our interest is to see whether the mean pattern correlations between the random errors and dominant FTNMs increase further with time above the values obtained for six-day periods (Figs. 7 and 10).

6.1 *Statistics of ensemble error growth for 8 to 14 November*

We again study the statistics of the growth of 100 initial, randomly generated error fields constructed as described in section 4 on 8 November. Their evolution is analyzed for the period 8–14 November, which covers the time interval of the development, maturation and decay of the Indian Ocean block. The standard deviations of the 100 evolved error fields are calculated on each day and shown on 12 and 14 November in Figs. 11a and 11b respectively. By 12 November we note that the error fields are concentrated in, and downstream of, the blocking region in the Indian Ocean (Fig. 11a), with a second major center over southern South America. On subsequent days

Table 3. Nondimensional real (λ_r) and imaginary (λ_i) parts of eigenvalues, amplification factors($|\ \lambda\ |$), the dimensional growth rates ($\omega_{d,\,i}$) and e-folding times (τ) of FTNM 1 during 05–11 December 1989 (viscous case).

Basic state	λ_r	λ_i	$\|\ \lambda\ \|$	$\omega_{d,\,i}$ (d^{-1})	τ (d)
05–06	1.093	–0.578	1.236	0.211	4.939
05–07	1.040	–1.169	1.565	0.223	4.485
05–08	1.989	0.0	1.989	0.229	4.375
05–09	1.884	0.0	1.884	0.158	6.337
05–10	–0.941	2.036	2.243	0.161	6.210
05–11	1.190	–2.004	2.331	0.141	7.110

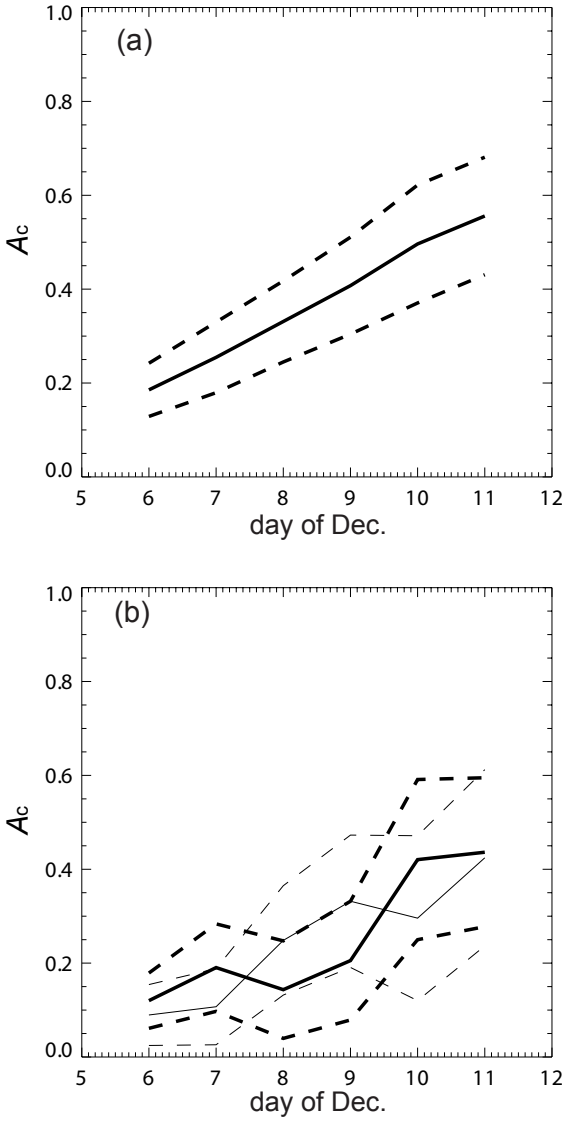

Fig. 10. Pattern correlations (A_c) between the dominant FTNMs and the 100 evolved random errors in the viscous case during the periods starting on 5 and finishing on 6, 7, ..., 11 December 1989 respectively. (a). The mean (thick solid) and the mean ± the standard deviation of the largest correlations taken over the five fastest growing FTNMs (thick dashed) are shown. (b). The mean (solid) and mean ± standard deviation (dashed) of correlations between the 100 evolved random errors and FTNM 1 (thick) or FTNM 2 (thin).

the maximum standard deviation of the error fields drifts down-stream and amplifies as the block starts to decay (Fig. 11b). The major centers of the standard deviation error field again occur in the regions of rapid dynamical development.

Figures 11c and 11d show the fastest growing FTNMs for the periods 8–12 and 8–14 November respectively. These FTNMs are dipole or multi-pole wave train disturbances with similar scale to the block; they have largest amplitude in, and downstream of, the blocking region. Comparing the FTNMs with the standard deviations of the error fields, we see that on respective days both quantities have largest amplitudes in the same regions. The dynamical diagnostics for these FTNMs are shown in Table 4; displayed are the eigenvalues, amplification factors, dimensional growth rates and e-folding times. The amplification factors shown there are fairly similar to those in Table 2 for April for the same respective time intervals. In April, we found that only one out of the 100 initial

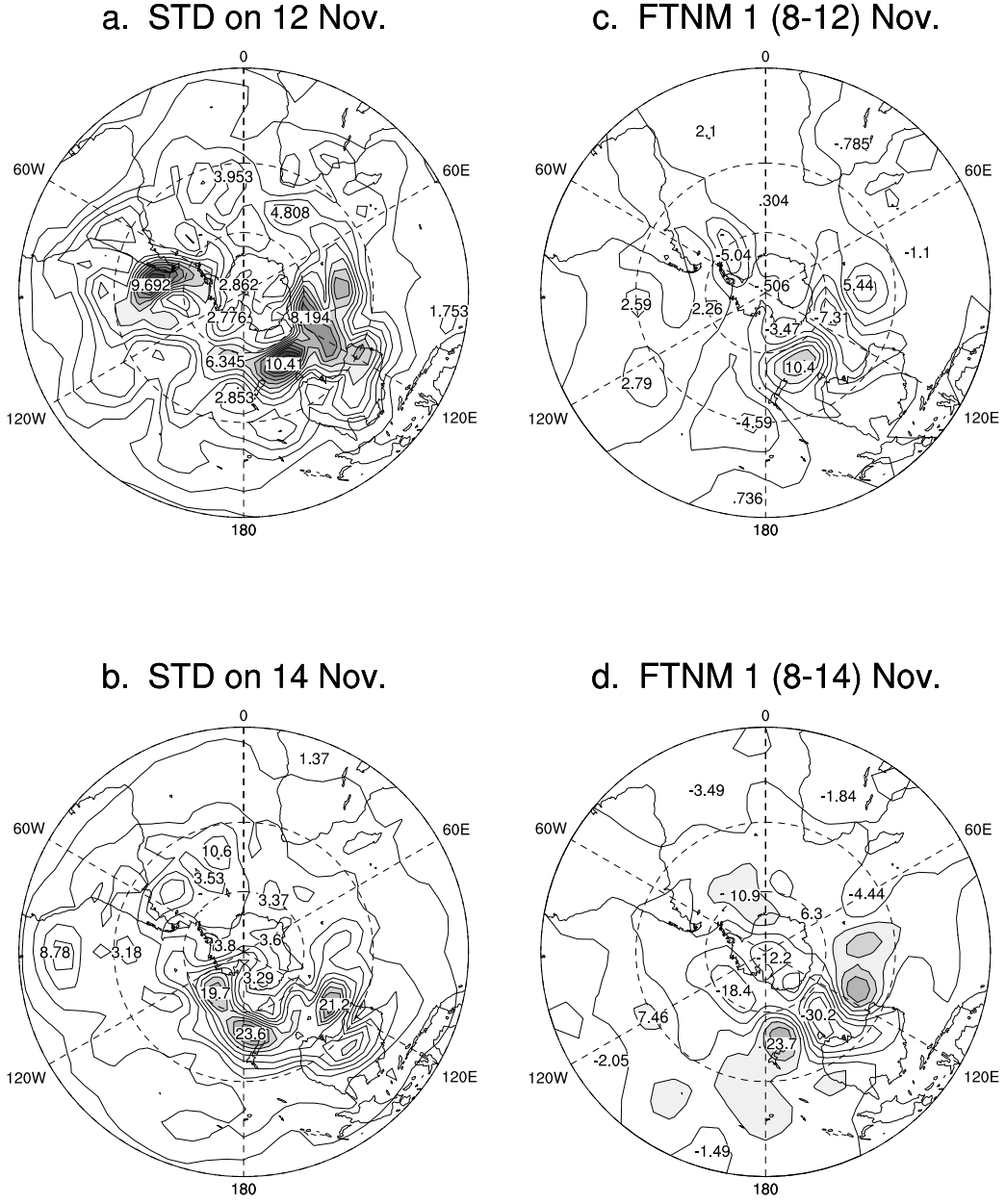

Fig. 11. The standard deviations of the 100 evolved random errors on 12 November (a) and 14 November (b) 1989 for the viscous case. Shown are FTNM 1 for the periods 8–12 November (c) and 8–14 November (d) 1989 in the viscous case.

error fields grew faster than FTNM 1 (after 2 days of development). For November, we have found that only one out of the 100 initial error fields grows faster than FTNM 1, after four days of development, and three grow faster than FTNM 1 after five days of development. On the whole, it is improbable that initial random errors will grow faster than FTNM 1.

Figure 12 shows the mean (solid) and mean ± the standard deviation (dashed) of the pattern correlations between each of the 100 error fields and FTNMs on successive days. Figure 12a (thick lines) displays these statistics for the largest correlations taken over the five fastest growing FTNMs for periods starting on 8 November and ending on subsequent successive days up until 14 November. The corresponding statistics for correlations between error fields and FTNM 1 are also shown in this figure (thin lines).

Again, the statistics in thick lines in Fig. 12a increase monotonically with time and the mean has reached a value greater than 0.6 after six days. The mean of the pattern correlations between the error fields and FTNM 1 again tend to increase with time but not monotonically indicating on some days, e.g., 13 November, a sub-dominant FTNM yields the largest mean of the pattern correlations. Our results here are quantitatively similar to the respective results for April (Fig. 7) and December (Fig. 10).

Next, we analyze probability distributions of correlations between the 100 evolved error fields on 14 November and FTNMs for the period 8 to 14 November. Figure 13a displays the probability distribution for the largest correlations taken over the five fastest growing FTNMs, while Fig. 13b shows the distribution for correlations with FTNM 1. In both cases, the peak in the probability distributions occur at pattern correlations slightly larger than $A_c = 0.6$. The mean of the correlations taken over the five fastest growing FTNMs is 0.636 and the mean of the correlations with FTNM 1 is 0.592.

Table 4. Nondimensional real (λ_r) and imaginary (λ_i) parts of eigenvalues, amplification factors($|\ \lambda\ |$), the dimensional growth rates ($\omega_{d,\,i}$) and e-folding times (τ) of FTNM 1 during 08–14 November 1989 (viscous case).

Basic state	λ_r	λ_i	$\|\lambda\|$	$\omega_{d,\,i}$ (d^{-1})	τ (d)
08–09	0.927	–0.732	1.181	0.166	6.020
08–10	1.334	0.0	1.334	0.144	6.959
08–11	1.630	0.0	1.630	0.162	6.160
08–12	–0.286	1.931	1.952	0.167	5.999
08–13	2.239	0.0	2.239	0.161	6.225
08–14	–2.795	1.212	3.047	0.185	5.403

6.2 *Statistics of ensemble error growth for 1 to 15 November*

In this subsection, we analyze the growth of initial

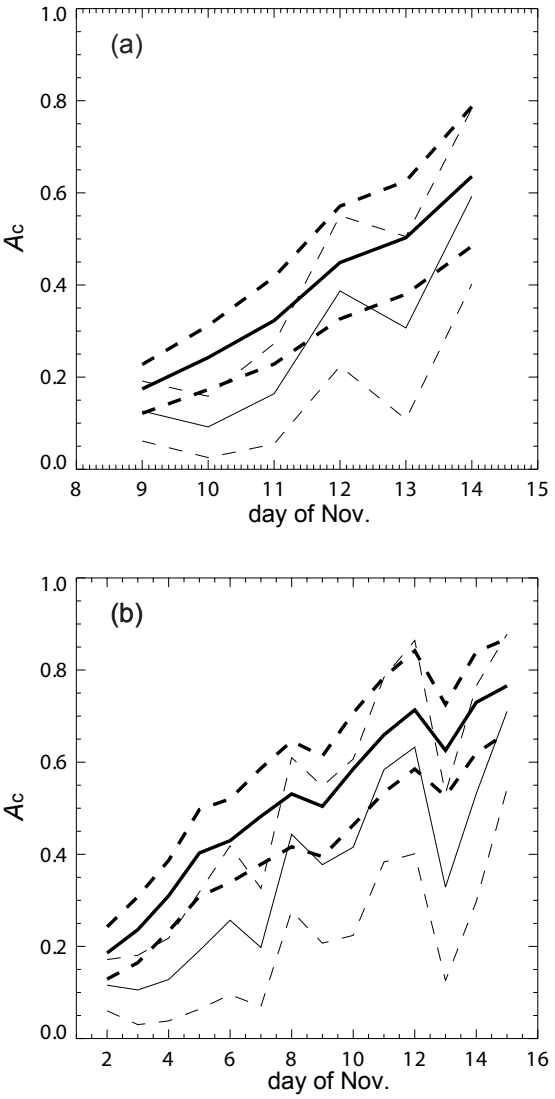

Fig. 12. The mean and mean ± the standard deviation of the pattern correlations between each of the 100 error fields and FTNMs in November in viscous case. (a). The mean (thick solid line) and mean ± the standard deviation (thick dashed lines) of the largest pattern correlations taken over the five fastest growing FTNMs for periods starting on 8 November and ending on subsequent successive days up until 14 November. The mean (thin solid line) and mean ± the standard deviation (thin dashed lines) of the pattern correlations between the 100 evolved error fields and FTNM 1 for the same periods. (b). As in (a) but for the periods starting on 1 November and ending on subsequent successive days up until 15 November.

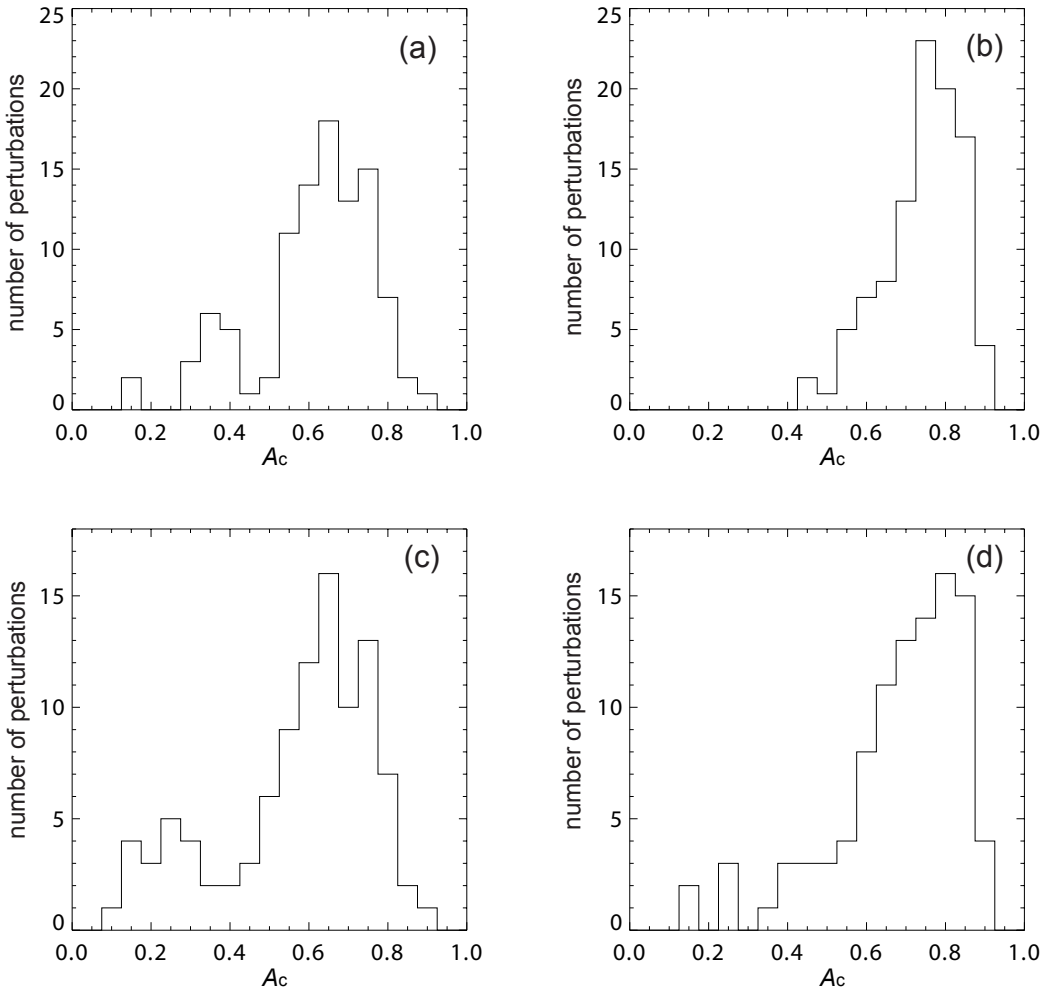

Fig. 13. The probability distributions of correlations between the 100 evolved random errors on 14 and 15 November and FTNMs for the periods 8–14 and 1–15 November for the viscous case. (a) The probability distributions for the largest correlations taken over the five fastest growing FTNMs during 8–14 November. (b) The probability distributions for the correlations with FTNM 1 during 8–14 November. (c) The same as (a), but for 1–15 November. (d) The same as (b), but for 1–15 November.

random errors over the longer time period than the six days considered in the previous sections and in subsection 6.1. We consider the period between 1 and 15 November with the 100 random error fields initialized on 1 November. We have calculated standard deviation fields of the 100 evolved error fields on each day from 1 to 15 November; we find that these standard deviations on 12, 13 and 14 November are quite similar in structure to those in Figs. 11a–c respectively, even though the random fields are generated much earlier (not shown). The standard deviation field is focussed in the section between 60°E and 120°E by 7 November (not shown) as the Indian Ocean block starts to develop (Fig. 1b). Thereafter, its evolution is quite similar to the description given in section 6.1.

Figure 12b also shows the mean (solid) and mean ± standard deviation (dashed) of the pattern correlations between the 100 error fields and FTNMs on successive days during the period 1 to 15 November. The statistics for the largest correlations taken over the five fastest growing FTNMs, and the statistics for correlations between the error fields and FTNM 1, are displayed in thick and thin lines respectively. We note that the increase in the mean correlations over the first six days to 7 November is less in Fig. 12b than it is over the six days to 14 November in Fig. 12a respectively. This is related to the different stability of the basic state during the respective periods. The formation and decay of the Indian Ocean block in the second week of November is associated with rapid er-

ror growth, while in the first week of November the flow is less unstable. We have confirmed this by analyzing the amplification factors in these periods (not shown). Thus, errors will tend to grow faster in the second week and converge more rapidly to the dominant FTNMs than during the first week.

Figure 13 also shows probability distributions of correlations between the 100 evolved error fields (initialized on 1 November) on 15 November and FTNMs for the period 1–15 November. Figure 13c shows the probability distribution for the largest correlations taken over the five fastest growing FTNMs and Fig. 13d gives the distribution for correlations with FTNM 1. We see a significant shift to larger values of pattern correlation in the right panel histograms compared with the left histograms in Fig. 13. The mean associated with the distribution in Fig. 13c is 0.766, while for that in Fig. 13d, it is 0.710.

7. Discussion and conclusions

We have examined the structural organization of initial random errors evolving in a barotropic tangent linear model. The time-dependent basic state used has been obtained by linear interpolation of daily 300 hPa analysis fields. This ensures that the error fields see a basic state that closely follows the truth throughout its development. This is not generally possible using basic states taken from a nonlinear model forecast since the flow fields in such a model will generally begin to diverge from the analyses within a few days.

We have concentrated on studies of error growth during periods of block development, maturation and decay in the Southern Hemisphere in April, November and December 1989. The growth of initial random errors during each of these periods of blocking has been analyzed. Our particular aim has been to study the statistics of the growth of 100 initially random error fields in these synoptic situations. We have compared the structures of evolved error fields with the structures of normal modes, and in particular, FTNMs.

During April, we have shown by means of a case study that an initial, random error field is organized by the tangent linear dynamics to take up dipole or multi-pole structures of similar scales to the blocks, and which are focussed in the respective blocking regions and extend downstream. After three to six days, the evolved error field is structurally somewhat similar to dominant normal modes of the instantaneous flow a short time before the day of interest. The evolved error field more closely resembles the dominant FTNMs calculated for the same period. As for the corresponding Northern Hemisphere cases of blocking (Frederiksen, 1998; Frederiksen and Bell, 1990), the dominant normal modes of the instantaneous flow characterize, to a first approximation, the structures of instability and error growth over the next one or two days. The dominant FTNMs, however, provide a more accurate representation of the structures of evolved errors due to the fact that the tangent linear dynamics provides a filtering of initial errors in favor of the dominant FTNMs (Frederiksen, 1997, 2000).

The qualitative results for the above case study for April have been confirmed by the statistics of 100 evolved error fields for each of the three cases of blocking in April, November and December. We have analyzed the increase with time of amplification factors of the error fields and compared them with some of the fastest growing FTNMs for the same time intervals. Most random errors have amplification factors that are close to, but slightly less than, those of the fastest growing FTNM. We find that the probability of the evolved error exceeding the FTNM 1 amplification (for the same period) is only a few percent. As the 100 error fields evolve, their maxima of standard deviations become focussed in the regions of rapid dynamical development, particularly associated with the developing and decaying blocks.

We have calculated the mean and standard deviations of the pattern correlations between each of the 100 evolved error fields and the five fastest growing FTNMs (for the same time interval). The mean of the largest pattern correlation taken over the five fastest growing FTNMs increases with increasing time interval reaching a value close to $A_c = 0.6$ or larger after six days. The mean of the pattern correlations with individual dominant FTNMs also generally increases with time but not always monotonically. FTNM 1 generally, but not always, gives the largest mean pattern correlation with the error fields. Pattern correlations, taken over the five fastest growing normal modes and with normal mode 1, tend to be lower than with the respective FTNMs. However, they are significant and suggest that truncated expansions in terms of the faster growing normal modes may provide reasonable representations of evolved error fields (Frederiksen and Bell, 1990; Anderson, 1996; Frederiksen, 1998). We have also compared probability distributions of correlations between the 100 evolved error fields and the dominant FTNMs and dominant normal modes. These confirm the above conclusions.

For November, we have compared the statistics of ensemble error growth for the 6-day period from 8 to 14 November with the longer 14-day period from 1 to 15 November. As expected, the final mean pattern correlations between the 100 evolved error fields and dominant FTNMs are larger for the longer period. The

mean of the largest pattern correlations, taken over the five fastest growing FTNMs, is 0.766 for the 14-day period compared with 0.636 for the 6-day period. Similarly, the mean correlations with FTNM 1 are 0.710 and 0.592 respectively. Our findings confirm the close correspondence between instability, error growth and dynamical developments noted in earlier works (e.g., Frederiksen and Bell, 1990; Kimoto, 1992). During the first week of November, error growth is less rapid than in the second week when the Indian Ocean block develops, matures and then decays. The faster error growth in the second week results in more rapid convergence to the dominant FTNMs.

In a sequel to this work, we compare the growth of initially random errors during Southern Hemisphere blocking with the growth and structures of evolved singular vectors and Lyapunov vectors.

Acknowledgments. It is a pleasure to thank Steve Kepert for assistance with this work. We thank Dr. J. Anderson of Geophysical Fluid Dynamics Laboratory (GFDL), Princeton and Prof. I. Goldhirsch of Tel-Aviv University for helpful e-mail communications on iterative solvers.

APPENDIX

Iterative eigensolvers

The iterative eigensolvers that we have developed are based on the Arnoldi method (Arnoldi, 1951), which can be used to generate some of the leading NMs of $\boldsymbol{M}$ in Eq. (4) when the basic state is stationary and to generate the dominant FTNMs of $\boldsymbol{G}$ in Eq. (5) for a time-varying basic state. The basic point of Arnoldi methods (Goldhirsch, 1987; Anderson, 1991) is to reduce the size of the matrix that needs to be solved to one only involving the most rapidly growing eigenvectors. For the case when the matrix $\boldsymbol{M}$ is a constant, the sub-dominant eigenvectors are purged by simply integrating the linear Eq. (4) forward for a sufficiently long time from a random initial condition. If the perturbation becomes too large after a certain time, then the perturbation is normalized and the integration continued. This process is repeated until the integrated perturbation is dominated by the leading eigenvectors of $\boldsymbol{M}$. In the case when $\boldsymbol{M}(t)$ is time dependent, the purging is achieved by integrating an initially random perturbation from t_0 to t, then recycling the perturbation back to t_0, integrating to t and continuing the process until the sub-dominant finite-time eigenvectors have been purged. In both cases, the final filtered perturbation vector is used to start the Arnoldi process.

For both constant and time-dependent $\boldsymbol{M}(t)$, the final filtered vector is denoted by $\boldsymbol{x}$. From this vector we then create k vectors, $\boldsymbol{x}_1 = \boldsymbol{x}$, $\boldsymbol{x}_2 = \boldsymbol{G}\boldsymbol{x}$, ..., $\boldsymbol{x}_k = \boldsymbol{G}^{k-1}\boldsymbol{x}$ where $\boldsymbol{G} = \boldsymbol{G}(t_0, t_0 + \Delta t)$ for the case when $\boldsymbol{M}$ is constant. The leading eigenpairs of $\boldsymbol{M}$ are independent of Δt. When $\boldsymbol{M}(t)$ is time dependent, we have $\boldsymbol{G} = \boldsymbol{G}(t_0, t)$. The subspace spanned by these k vectors is called the Krylov subspace; $K_k(\boldsymbol{G}, \boldsymbol{x}) = span\{\boldsymbol{x}, \boldsymbol{G}\boldsymbol{x}, \boldsymbol{G}^2\boldsymbol{x}, \ldots, \boldsymbol{G}^{k-1}\boldsymbol{x}\}$ where $\boldsymbol{G}$ is of dimension $n \times n$ and $k \ll n$ in general. One can then extract approximations for $\boldsymbol{G}$ from this k-dimensional subspace $K_k(\boldsymbol{G}, \boldsymbol{x})$.

We start the Arnoldi process from an initially normalized vector $\boldsymbol{w}_1 = \boldsymbol{x}(t)/||\boldsymbol{x}(t)||$, where $\boldsymbol{x}(t)$ is the final filtered vector discussed above that is dominated by the leading modes. The general terms in the factorization are determined through the coupled equations

$$\boldsymbol{v}_{i+1} = \boldsymbol{G}\boldsymbol{w}_i - \sum_{j=1}^{i} (\boldsymbol{w}_j^T \cdot \boldsymbol{G}\boldsymbol{w}_i)\boldsymbol{w}_j,$$

$$\boldsymbol{w}_{i+1} = \frac{\boldsymbol{v}_{i+1}}{||\boldsymbol{v}_{i+1}||}, \quad i = 1, 2, \ldots, k. \tag{19}$$

Each of the vectors $\boldsymbol{u}_i = \boldsymbol{G}\boldsymbol{w}_i$ is orthonormalised to all those previously generated. It can be shown that $\{\boldsymbol{w}_1, \boldsymbol{w}_2, \ldots, \boldsymbol{w}_k\}$ forms an orthonormal basis of the Krylov subspace K_k. We have used a modified Gram-Schmidt scheme, always with double orthogonalization (Saad, 1992).

Let $\boldsymbol{W}$ be the $n \times k$ matrix with column vectors $\{\boldsymbol{w}_1, \boldsymbol{w}_2, \ldots, \boldsymbol{w}_k\}$, then a by-product of the Arnoldi process is a small upper Hessenberg matrix $\boldsymbol{H}$ with dimension $k \times k$ where $\boldsymbol{H} = \boldsymbol{W}^{\mathrm{T}}\boldsymbol{G}\boldsymbol{W}$. The process can be described by

$$\boldsymbol{G}\boldsymbol{W} - \boldsymbol{W}\boldsymbol{H} = \boldsymbol{H}_{k+1,k}\boldsymbol{w}_{k+1}\boldsymbol{e}_k^{\mathrm{T}}, \tag{20}$$

where T denotes the transpose, $\boldsymbol{e}_k$ is a vector or $k \times 1$ matrix, with elements $e_k(i) = \delta_{ik}$. The eigenvalues and eigenvectors of $\boldsymbol{H}$ can be computed by any standard method, i.e., $\boldsymbol{H}y_i = \lambda_i y_i, \quad i = 1, 2, \ldots, k$. Here λ_i and y_i are the eigenvalues and eigenvectors of $\boldsymbol{H}$ respectively. The Ritz eigenvalues and Ritz eigenvectors are defined as λ_i and ϕ_i respectively (Saad, 1992), where ϕ_i is given by

$$\phi_i = \boldsymbol{W}y_i. \tag{21}$$

Some of the λ_i and ϕ_i constitute good approximate eigenvalues and eigenvectors of $\boldsymbol{G}$. In order to see the extent to which the eigenpairs of $\boldsymbol{G}$ can be obtained from these Ritz eigenvalues and eigenvectors, we multiply both sides of (20) by y_i yielding $\boldsymbol{G}\boldsymbol{W}y_i - \boldsymbol{W}\boldsymbol{H}y_i = \boldsymbol{H}_{k+1,k}\boldsymbol{w}_{k+1}\boldsymbol{e}_k^{\mathrm{T}}y_i$, which can be further written as

$$||(\boldsymbol{G} - \lambda_i I)\phi_i||_2 = \boldsymbol{H}_{k+1,k}|\boldsymbol{e}_k^{\mathrm{T}}y_i| = \boldsymbol{H}_{k+1,k}|y_{i,(k)}|. \tag{22}$$

Expression (22) indicates that the residual norm is equal to the last component of the eigenvector y_i multiplied by $\boldsymbol{H}_{k+1,k}$. From our experience in testing and using the solver, we find that this is a very good indicator of the actual error.

For both NMs and FTNMs, a chosen number of the fastest growing modes are calculated and we have found that time steps of $\Delta t = 450$ s or 900 s are suitable choices in our studies. We have checked our results by comparing them with those calculated by using Linear Algebra PACKage (LAPACK) subroutines.

REFERENCES

Anderson, J. L., 1991: The robustness of barotropic unstable modes in a zonally varying atmosphere. *J. Atmos. Sci.*, **48**, 2393–2410.

Anderson, J. L., 1993: The climatology of blocking in a numerical forecast model. *J. Climate*, **6**, 1041–1056.

Anderson, J. L., 1996: Selection of initial conditions for ensemble forecasts in a simple perfect model framework. *J. Atmos. Sci.*, **53**, 22–36.

Arnoldi, W. E., 1951: The principle of minimized iterations in the solution of the matrix eigenvalue problem. *Quarterly of Applied Mathematics*, **9**, 17–29.

Bengtsson, L., 1981: Numerical prediction of atmospheric blocking: A case study. *Tellus*, **33**, 19–24.

Borges, M. D., and D. L. Hartmann, 1992: Barotropic instability and optimal perturbations of observed nonzonal flows. *J. Atmos. Sci.*, **49**, 335–354.

Buizza, R. and F. Molteni, 1996: The role of finite-time barotropic instability during transition to blocking. *J. Atmos. Sci.*, **53**, 1675–1697.

Buizza, R., P. Houtekamer, Z. Toth, G. Pelerin, Mozheng Wei, and Y. Zhu, 2005: A comparison of the ECMWF, MSC and NCEP global ensemble prediction systems. *Mon. Wea. Rev.*, in press.

CMB, 1989: Climate Monitoring Bulletin, Southern Hemisphere, No. 39 April; No. 46, November; No.47, December 1989, National Climate Centre, Bureau of Meteorology, Australia.

Colucci, S. J. and D. P. Baumhefner, 1992: Initial weather regimes as predictors of numerical 30-day mean forecast accuracy. *J. Atmos. Sci.*, **49**, 1652–1671.

Coughlan, M. L., 1983: A comparative climatology of blocking action in the two hemispheres. *Australian Meteorological Magazine*, **31**, 3–13.

de Pondeca, M. S. F. A., A. Barcilon, and X. Zou, 1998a: An adjoint sensitivity study of the efficacy of modal and nonmodal perturbations in causing model block onset. *J. Atmos. Sci.*, **55**, 2095–2118.

de Pondeca, M. S. F. A., A. Barcilon, and X. Zou, 1998b: The role of wave breaking, linear instability, and PV transports in model block onset. *J. Atmos. Sci.*, **55**, 2852–2873.

Errico, R. M., T. Vukicevic, and K. Raeder, 1993: Examination of the accuracy of a tangent linear model. *Tellus*, **45A**, 462–477.

Farrell, B. F., 1989: Optimal excitation of baroclinic waves. *J. Atmos. Sci.*, **46**, 1193–1206.

Frederiksen, J. S., 1982: A unified three-dimensional instability theory of the onset of blocking and cyclogenesis. *J. Atmos. Sci.*, **39**, 970–982.

Frederiksen, J. S., 1984: The onset of blocking and cyclogenesis in Southern Hemisphere synoptic flows: Linear theory. *J. Atmos. Sci.*, **41**, 1116–1131.

Frederiksen, J. S., 1997: Adjoint sensitivity and finite-time normal mode disturbances during blocking. *J. Atmos. Sci.*, **54**, 1144–1165.

Frederiksen, J. S.; 1998: Precursors to blocking anomalies: The tangent linear and inverse problems. *J. Atmos. Sci.*, **55**, 2419–2436.

Frederiksen, J. S., 2000: Singular vectors, finite-time normal modes and error growth during blocking. *J. Atmos. Sci.*, **57**, 312–333.

Frederiksen, J. S., and R. C. Bell, 1990: North Atlantic blocking during January 1979: Linear theory. *Quart. J. Roy. Meteor. Soc.*, **116**, 1289–1313.

Frederiksen, J. S., and G. Branstator, 2001: Seasonal and intraseasonal variability of large-scale barotropic modes. *J. Atmos. Sci.*, **58**, 50–69.

Frederiksen, J. S., M. A. Collier, and A. B. Watkins, 2004: Ensemble prediction of blocking regime transitions. *Tellus*, **56A**, 485–500.

Goldhirsch, I., S. A. Orszag, and B. K. Maulik, 1987: An efficient method for computing leading eigenvalues and eigenvectors of large asymmetric matrices. *J. Sci. Computing.*, **2**, 33–58.

Held, I. M., 1983: Stationary and quasi-stationary eddies in the extratropical troposphere: Theory. *Large Scale Dynamic Processes in the Atmosphere*, B.J.Hoskins and R.P.Pearce, Eds., Academic Press, 127–167.

Houtekamer, P. L., and J. Derome, 1995: Methods for ensemble prediction. *Mon. Wea. Rev.*, **123**, 2181–2196.

Kimoto, M., H. Mukougawa, and S. Yoden, 1992: Medium-range forecast skill variation and blocking transition: A case study. *Mon. Wea. Rev.*, **120**, 1616–1627.

Lacarra, J. F., and O. Talagrand, 1988: Short-range evolution of small perturbations in a barotropic model. *Tellus*, **40A**, 81–95.

Legras, B., and R. Vautard, 1996: A guide to Liapunov vectors. *Proc. of a Seminar Held at ECMWF on Predictability*, 4–8 September 1995, Vol.I, 143–156.

Lejenas, H., 1984: Characteristics of southern hemisphere blocking as determined from a time series of observational data. *Quart. J. Roy. Meteor. Soc.*, **110**, 967–979.

Lorenz, E. N., 1965: A study of the predictability of a 28-variable atmospheric model. *Tellus*, **17**, 321–333.

Molteni, F., and T. Palmer, 1993: Predictability and finite-time instability of the northern winter circulation. *Quart. J. Roy. Meteor. Soc.*, **119**, 269–298

Molteni, F., R. Buizza, T. Palmer, and T. Petroliagis, 1996: The ECMWF ensemble prediction system: Methodology and validation. *Quart. J. Roy. Meteor. Soc.*, **122**, 73–119

Mu, M., and W. Duan, 2003: A new approach to studying ENSO predictability: Conditional nonlinear optimal perturbation. *Chinese Sci. Bull.*, **48**, 1045–1047.

Mu, M., W. S. Duan, and B. Wang, 2003: Conditional nonlinear optimal perturbation and its applications. *Nonlinear Process in Geophysics*, **10**, 493–501.

Noar, P. F., 1983: Numerical modelling of blocking with reference to June 1982. *Australian Meteorological Magazine*, **31**, 37–49.

Noone, D., and I. Simmonds, 1998: Similarity of "fast-growing perturbations" and an illustrative experiment with ensemble forecasting. *Australian Meteorological Magazine*, **47**, 5–19.

Palmer, T. N., 1993: Extended-range atmospheric prediction and the Lorenz model. *Bull. Amer. Meteor. Soc.*, **74**, 49–65.

Saad, Y., 1992: *Numerical Methods for Large Eigenvalue Problems*. Halsted Press-John Wiley & Sons Inc., 346pp.

Simmons, A. J., J. M. Wallace, and G. W. Branstator, 1983: Barotropic wave propagations and instability, and atmospheric teleconnection patterns. *J. Atmos. Sci.*, **40**, 1363–1392.

Szunyogh, I., E. Kalnay, and Z. Toth, 1997: A comparison of Lyapunov and Optimal vectors in a low-resolution GCM. *Tellus*, **48A**, 200–227.

Tibaldi, S., and F. Molteni, 1990: On the operational predictability of blocking. *Tellus*, **42A**, 343–365.

Tibaldi, S., P. Ruti, and M. Maruca, 1995: Operational predictability of winter blocking at ECMWF: An update. *Ann. Geophysicae*, **13**, 305–317.

Toth, Z., and E. Kalnay, 1993: Ensemble forecasting at NMC: the generation of perturbations. *Bull. Amer. Meteor. Soc.*, **174**, 2317–2330.

Toth, Z., and E. Kalnay, 1997: Ensemble forecasting at NCEP and the breeding method. *Mon. Wea. Rev.*, **125**, 3297–3319.

Tribbia, J., and D. Baumhefner, 1993: On the problem of prediction beyond the deterministic range. *Proc. NATO Workshop on Predictions of Interannual Climate Variations*, S. Shukla, Ed., NATO ASI Series, Springer-Verlag, 251–265.

van Loon, H., 1956: Blocking action in the Southern Hemisphere, Part I. *Notos*, **5**, 171–177.

Veyre, P., 1991: Direct prediction of error variances by the tangent linear model: A way to forecast uncertainty in the short range? *Proc. ECMWF Workshop on New Developments in Predictability*, Reading, UK, 65–86.

Wei, Mozheng, 2000: Quantifying local instability and predictability of chaotic dynamical systems by means of local metric entropy, *International Journal of Bifurcation and Chaos*, **10**, No.1, 135–154.

Wei, Mozheng, and Z. Toth, 2003: A New Measure of Ensemble Performance: Perturbation versus Error Correlation Analysis (PECA). *Mon. Wea. Rev.*, **131**, 1549–1565.

Whitaker, J. S., and A. Barcilon, 1992: Type B cyclogenesis in zonally varying flow. *J. Atmos. Sci*, **49**, 1877–1892.

Wright, A. D. F., 1974: Blocking action in the Australian region. Tech. Rep., No. 10, Bureau of Meteorology, Australia, 29pp.